

Supporting information

Proton-enabled biomimetic stabilization of small-molecule organic cathode in aqueous zinc-ion batteries

Nhu T. H. Luu,^[a] Alexander S. Ivanov,^{*,[b]} Teng-Hao Chen,^[c] Ilja Popovs,^[b]
Jui-Chin Lee^[d] and Watchareeya Kaveevivitchai^{*,[a]}

[a] Department of Chemical Engineering
and Hierarchical Green-Energy Materials Research Center
National Cheng Kung University
No.1 University Rd., Tainan City 70101, Taiwan

[b] Chemical Sciences Division, Oak Ridge National Laboratory
Oak Ridge, P.O. Box 2008, TN 37831, USA

[c] School of Pharmacy, National Cheng Kung University
No.1 University Rd., Tainan City 70101, Taiwan

[d] Core Facility Center
National Cheng Kung University
No.1 University Rd., Tainan City 70101, Taiwan

*To whom correspondence should be addressed. E-mail: ivanova@ornl.gov,
wkaveechai@mail.ncku.edu.tw

General methods and materials

Starting materials and solvents were purchased and used without further purification from commercial suppliers (Sigma-Aldrich and Alfa Aesar). The compound HATAQ was prepared by a reaction between 2,3-diamino-1,4-naphthaquinone and cyclohexane hexaketone according to our original procedure reported previously.¹ Powder X-ray diffraction (PXRD) patterns were collected on Bruker D8 Advance ECO. Fourier-transform infrared (FT-IR) spectra were recorded on Nicolet iS5 or Nicolet 6700, Thermo Scientific. The Raman spectra of the samples were collected by UniDRON Raman microscope with an excitation laser beam wavelength of 633 nm. X-ray photoelectron spectroscopy (XPS) measurements were performed on ULVAC PHI 5000 VersaProbe III with Al K α (1487 eV) as an X-ray source. Survey scans were collected with a pass energy of 100 eV, followed by high-resolution scans of the C 1s, N 1s, and O 1s regions with a pass energy of 20 eV. All spectra were charge-corrected relative to the C 1s component at 284.5 eV binding energy and analyzed using CasaXPS software. Scanning electron microscopy (SEM) images were collected on a SU8010 HR-FESEM scanning electron microscope. Scanning transmission electron microscopy (STEM) and energy dispersive X-ray spectroscopy (EDS) were carried out on JEOL JEM-2010 electron microscope. The ¹H solid-state nuclear magnetic resonance (NMR) spectra were recorded on a Bruker Avance III HD 400MHz NMR.

Synchrotron X-ray scattering measurements

High-energy X-ray total scattering data were collected at the 28-ID-1 beamline of the National Synchrotron Light Source II (NSLS-II), Brookhaven National Laboratory. A horizontally focusing side bounce monochromator was used to deliver X-rays with the energy of 74.4 keV (0.1667 Å) and a beam of cross-sectional area 0.25×0.25 mm². An amorphous 2D silicon-based area detector (PerkinElmerXRD 1621, 200×200 micron pixels) was positioned about 20.8 cm from the sample to collect total scattering intensity data, which yielded an accessible momentum transfer (Q) range up to 32 Å⁻¹. Powder samples of the pristine HATAQ, fully discharged HATAQ electrode (washed with acetic acid), and Zn₄(OH)₆SO₄·5H₂O were enclosed in polyimide capillaries and measured in transmission mode at room temperature with a total measurement time of 10 min per sample. The dark current scans were collected and subtracted from the raw X-ray patterns, allowing to remove residual intensity and prevent pixel overexcitation.² Data for an empty polyimide container were also collected for the background correction. Calibration of the sample to detector distance and detector alignment with data from a LaB₆ powder (NIST 660C) standard was done in *pyFAI* software.³ Raw scattering data were radially integrated into Q-space spectra, applying a mask and polarization correction during integration using *xpdtools* package.⁴ The normalized

total scattering patterns – structure functions, $S(Q)$'s, were obtained in *PDFgetX2*⁵ by subtracting polyimide container scattering, employing the appropriate sample composition and corrections (sample self-absorption, multiple scattering, and inelastic Compton scattering) following standard procedures.^{6,7} The resultant real space pair distribution functions, $G(r)$ s, in Figures 1 and 2 (main text) were calculated via Fourier transformation (eq. 1) of the $S(Q)$ utilizing a Q_{\max} of 25 Å⁻¹.

$$G(r) = \frac{2}{\pi} \int_{Q_{\min}}^{Q_{\max}} Q[S(Q) - 1] \sin(Qr) dQ \quad (1)$$

Quantum chemical calculations

Electronic structure calculations of the HATAQ-H and HATAQ-Zn molecular complexes were performed with the Gaussian 16 rev A.03.⁸ We used the density functional theory (DFT) approach for our calculations at the B3LYP/def2-SVP level of theory. Frequency calculations were performed to ensure that optimized geometries were minima on the potential energy surface and to compute zero-point energies (ZPE) and thermal corrections (T = 298.15 K) to Gibbs free energy. The implicit SMD polarizable continuum model⁹ with water as the solvent (default settings) was used in the optimization procedure to describe aqueous environment of the electrolyte employed in the experiments. The calculations of the Gibbs free energy for the H/Zn complexation reaction require the global minimum geometries for HATAQ-H and HATAQ-Zn species. We performed an unbiased quantum-chemical search for the most energetically stable HATAQ complexes with H/Zn using the Coalescence Kick (CK) program,^{10,11} which employs a stochastic approach for finding the global minimum. Some additional structures not found by the CK algorithm were constructed, optimized and their relative energies were compared to confirm the lowest energy structure among other possible configurations.

Chemical bonding analysis was performed for the DFT optimized periodic structures of HATAQ, HATAQ-H, and HATAQ-6H using the natural bond orbital (NBO) methodology.¹² The donor-acceptor interaction energy (second-order stabilization energies, $E^{(2)}$) in the NBOs was estimated via second-order perturbation theory analysis of the Fock matrix.¹³ For each donor orbital (i) and acceptor orbital (j), the stabilization energy $E^{(2)}$ associated with $i \rightarrow j$ delocalization is given by:

$$E_{i,j}^{(2)} = -o_i \frac{\langle i | \hat{F}_{(i,j)} | j \rangle^2}{\varepsilon_j - \varepsilon_i}, \text{ where } o_i \text{ is the donor orbital occupancy, } \hat{F}_{(i,j)} \text{ is the Fock operator, and } \varepsilon_i \text{ and } \varepsilon_j \text{ are the orbital energies.}$$

Periodic DFT calculations were performed using the Vienna Ab-initio Simulation

Package (VASP).¹⁴⁻¹⁷ The valence electronic states were expanded in a basis of plane waves, while the core valence interactions were described using the Projector Augmented Wave (PAW) approach.^{18,19} The plane wave kinetic energy cut off was set to 600 eV and the PBE GGA functional²⁰ was employed to describe the exchange correlation interactions. The DFT-D3 approach of Grimme with zero damping²¹ was used to account for the van der Waals interactions. The SCF convergence threshold was set to 10^{-5} eV and a Pulay scheme²² was used for charge density mixing during the SCF solution. The chosen level of theory was shown to provide sufficient accuracy in predicting structural parameters for the HATAQ structure as compared to the experimental X-ray single-crystal diffraction results.¹

Electrochemical studies

To prepare electrodes, HATAQ (30 wt%), Ketjen black conductive carbon (60 wt%), and poly(vinylidenedifluoride) (PVDF) (10 wt%) were mixed and ground in the presence of *N*-methyl-2-pyrrolidinone (NMP). The mass loading of the active material was kept at ~ 0.7 mg (for 30 wt%). Other ratios of electrode mixture, 45:45:10 and 60:30:10, were also tested. The slurry was coated onto carbon paper (MGL280) current collector and dried overnight at 100 °C in vacuum. CR2032 coin cells were assembled by using Zn metal as anode, 1 M ZnSO₄ aqueous solution as electrolyte, and Whatman glass microfiber (GF/A) membrane as separator. Other Zn electrolytes (1 M Zn(CF₃SO₃)₂ in various solvent systems) were investigated to determine an optimized electrochemical performance. In addition, three-electrode cells with activated carbon (counter electrode), saturated calomel electrode (reference electrode), and HATAQ (working electrode) were employed to investigate the charge storage mechanism in three different electrolyte systems, 1 M ZnSO₄ in H₂O, 1 M H₂SO₄ in H₂O, and 1 M ZnSO₄ in D₂O. The galvanostatic charge/discharge and cyclic voltammetry measurements were carried out with a Neware battery cycler and a VMP3 system (BioLogic). Galvanostatic intermittent titration technique (GITT) was performed at current density of 80 mA g⁻¹ for 15 min followed by a 2 h relaxation. Electrochemical impedance spectroscopy (EIS) measurements were carried out over a frequency range of 1 kHz–1 mHz. The coin cells were allowed to rest for at least 30 min before measurements. For activation energy calculations, the cells were placed in a temperature chamber and EIS and GITT data were collected at 35, 40, 45, and 50 °C. The cells were allowed to equilibrate for at least 1 h at each temperature.

For all ex-situ analyses, the cells were cycled to various states of charge with a rate of 200 mA g⁻¹. The HATAQ electrodes for ex-situ Raman and FT-IR measurements contained 70 wt% active material, 20 wt% copper, and 10 wt% PVDF.²³ The ex-situ XPS, PXRD, and STEM-EDS were done on HATAQ electrodes consisted

of 70 wt% active material, 20 wt% Ketjen Black, and 10 wt% PVDF. Stainless steel was used as current collector for all these ex-situ experiments mentioned above. The coated electrodes were dried overnight at 100 °C in vacuum. For ex-situ SEM, the electrode mixture was prepared by using 30 wt% active material, 60 wt% Ketjen black, and 10 wt% PVDF and coated onto carbon paper MGL280. The self-standing electrodes (0.2 mm thick) for ex-situ ^1H solid-state NMR contained 30 wt% active material, 60 wt% copper, and 10 wt% poly(tetrafluoroethylene) (PTFE). The electrode mixture was combined together by using ethanol and the electrodes were dried in vacuum overnight at 80 °C. The coin cells were assembled by using Zn metal as anode, 1 M ZnSO_4 aqueous solution as electrolyte, and Whatman glass microfiber (GF/A) membrane as separator. For all the ex-situ measurements, the electrodes were cycled to various states of charge and the cells were disassembled. Unless otherwise noted, the electrodes were washed with DI water and dried in vacuum at 80 °C for 24 h prior to ex-situ measurements. To remove the zinc hydroxide sulfate (ZHS) from the surface, each electrode was washed by soaking in acetic acid for 10 s, followed by rinsing with DI water and drying in vacuum at 80 °C.

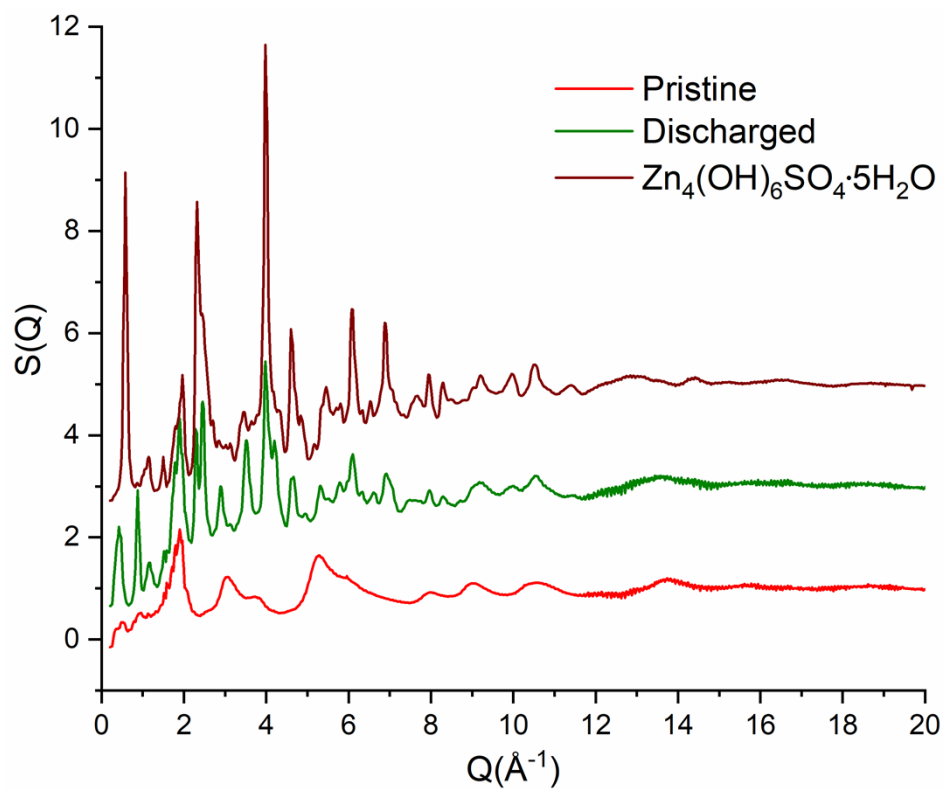


Fig. S1 Structure functions, $S(Q)$'s, for the pristine HATAQ (red), fully discharged HATAQ electrode (green), and $\text{Zn}_4(\text{OH})_6\text{SO}_4 \cdot 5\text{H}_2\text{O}$ (vine) samples.

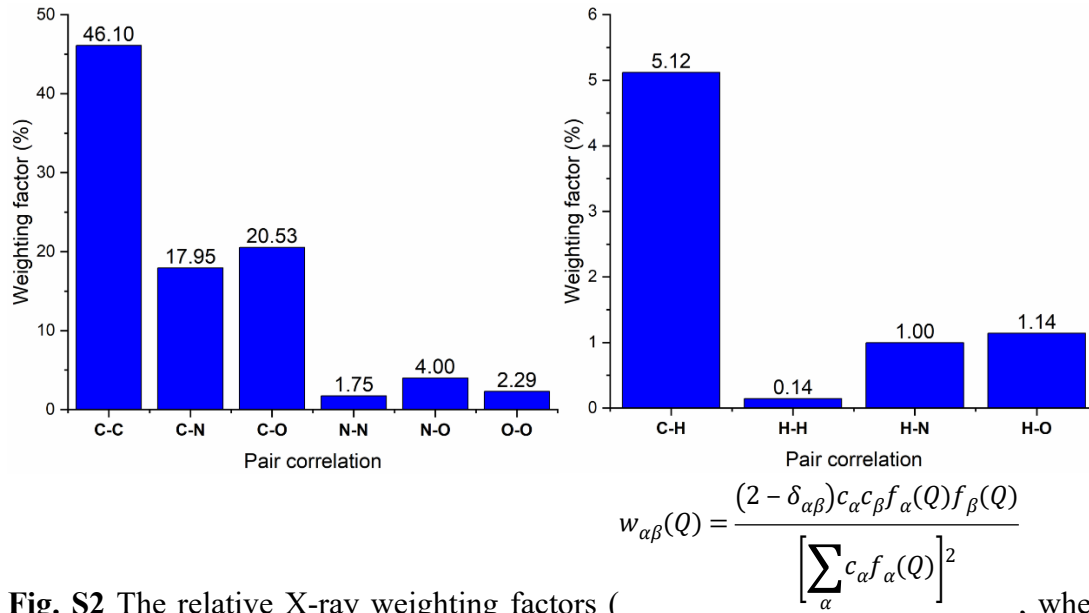


Fig. S2 The relative X-ray weighting factors (, where $f_{\alpha}(Q)$, $f_{\beta}(Q)$ are Q-dependent X-ray atomic form factors, c_{α} , c_{β} are molar fractions of species α and β , respectively, and $\delta_{\alpha\beta}$ is one for $\alpha=\beta$ and zero for $\alpha \neq \beta$) calculated at $Q = 0$ for the atomic pair correlations in the HATAQ system. As can be seen, most of the scattering comes from the pairs containing C, O, and N and thus the X-ray scattering patterns in Figure 1 (main text) are primarily dominated by C-C, C-N, and C-O correlations. Taking into account the relative X-ray weighting factors and integrating the first peak in the PDF (Figure 1, main text), we find that the average nearest-neighbor coordination number (CN) for C atoms is 2.7, which is in agreement with the average CN value of 2.67 for the HATAQ molecule (not counting neighboring H atoms in the terminal aromatic rings).

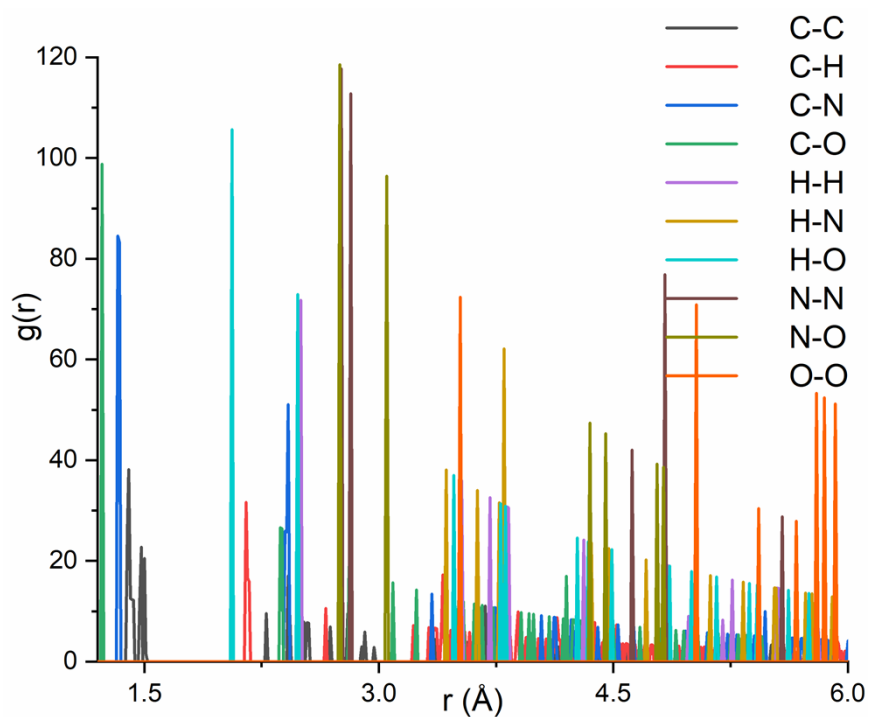


Fig. S3 Partial radial distribution functions, $g(r)$, (not X-ray weighted) from an ideal periodic structure of HATAQ. The peak corresponding to H-O atomic pair correlation (sky blue line) is centered at 2.06 Å.

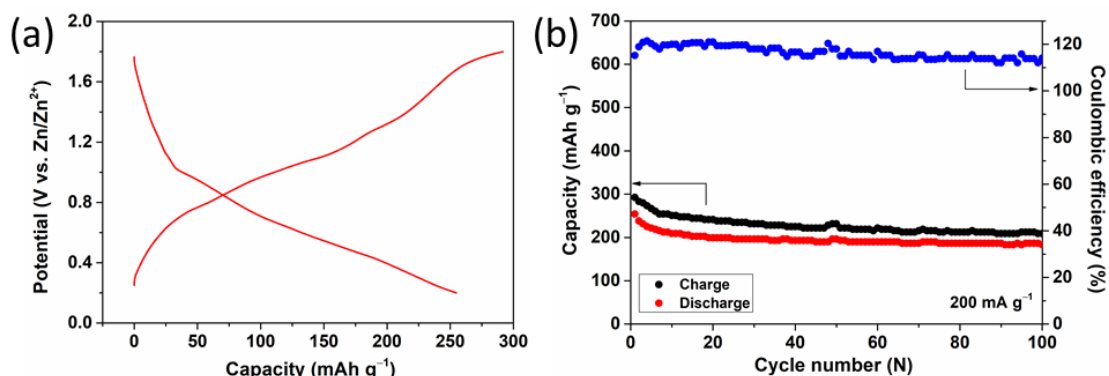


Fig. S4 (a) Voltage profile of HATAQ electrode with 1 M $\text{Zn}(\text{CF}_3\text{SO}_3)_2$ in acetonitrile (AN) as electrolyte and Zn metal as anode at the rate of 200 mA g^{-1} . (b) Capacity retention and Coulombic efficiency for the first 100 cycles. The result shows poor cycling stability of HATAQ in this organic electrolyte.

Preliminary zinc-ion battery performance testing was carried out using HATAQ as cathode with Zn metal as anode and 1 M $\text{Zn}(\text{CF}_3\text{SO}_3)_2$ solution in an organic, aqueous, and mixed solvent as electrolyte, respectively (Figure S4, S5). As expected without proton-enabled stabilization, in pure acetonitrile-based organic electrolyte, in addition to low overall battery performance, a more pronounced capacity fade as well as partial dissolution of HATAQ cathode material was observed upon cell cycling (72% of initial capacity remained after 100 cycles). In contrast, in the presence of water, a known proton source in mildly acidic electrolytes used in AZIBs, both pure aqueous and mixed electrolyte performed similarly, reaching 394 mAh g^{-1} capacity at the rate of 200 mA g^{-1} (Figure S5).

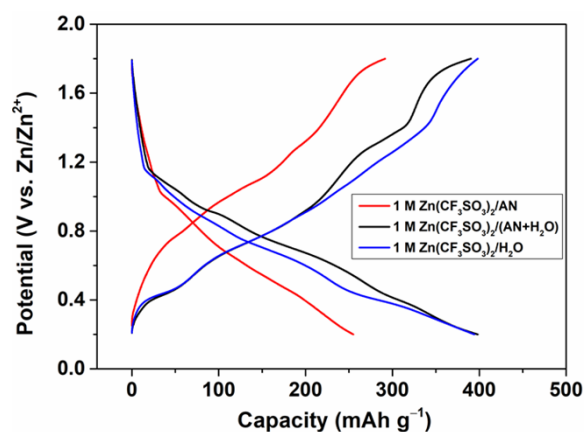


Fig. S5 (a) Voltage profiles of Zn/HATAQ cells at 200 mA g^{-1} in different $\text{Zn}(\text{CF}_3\text{SO}_3)_2$ electrolyte systems, with AN, H_2O , and 1:1 v/v AN/ H_2O as solvent.

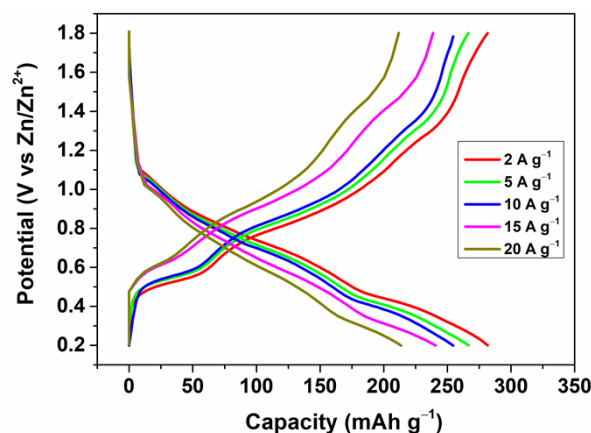


Fig. S6 Discharge/charge profiles of Zn/HATAQ cells at different current densities ranging from 2 to 20 A g⁻¹ in 1 M aqueous ZnSO₄ electrolyte.

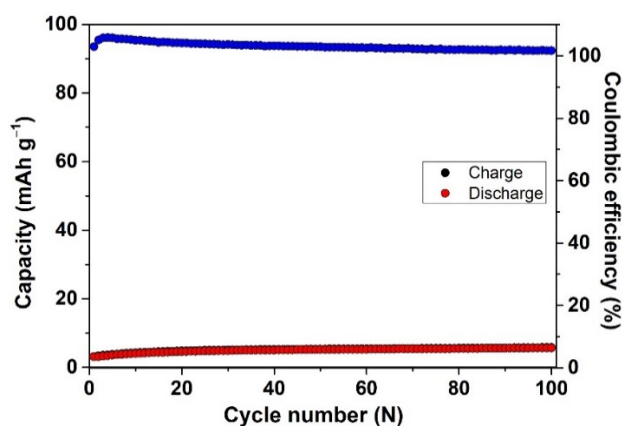


Fig. S7 Electrochemical properties of the conductive carbon (electrode ratio: Ketjen black : PVDF = 9 : 1, with mass loading of Ketjen black ~1.5 mg) at 200 mA g⁻¹ in 1 M ZnSO₄ aqueous solution as electrolyte and Zn metal as anode (red: discharge; black: charge). The delivered capacity of Ketjen black at this electrode ratio is estimated to be ~5 mAh g⁻¹ (between 0.2–1.8 V). At rates higher than 200 mA g⁻¹, the capacity contribution from Ketjen black is, therefore, considered to be almost negligible within this voltage window.

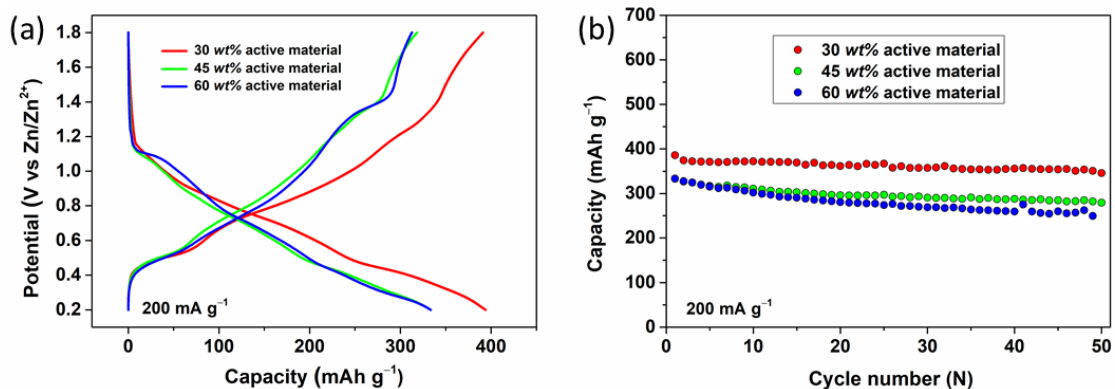


Fig. S8 (a) Discharge/charge profiles and (b) capacity retention plots of HATAQ electrodes with different amounts of active material at 200 mA g⁻¹ (PVDF was kept constant at 10 wt%).

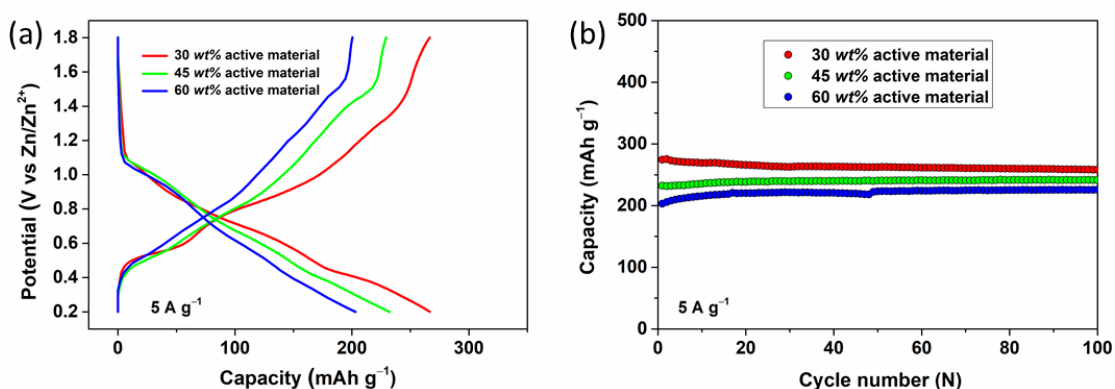


Fig. S9 (a) Discharge/charge profiles and (b) capacity retention plots of HATAQ electrodes with different amounts of active material at 5 A g⁻¹ (PVDF was kept constant at 10 wt%).

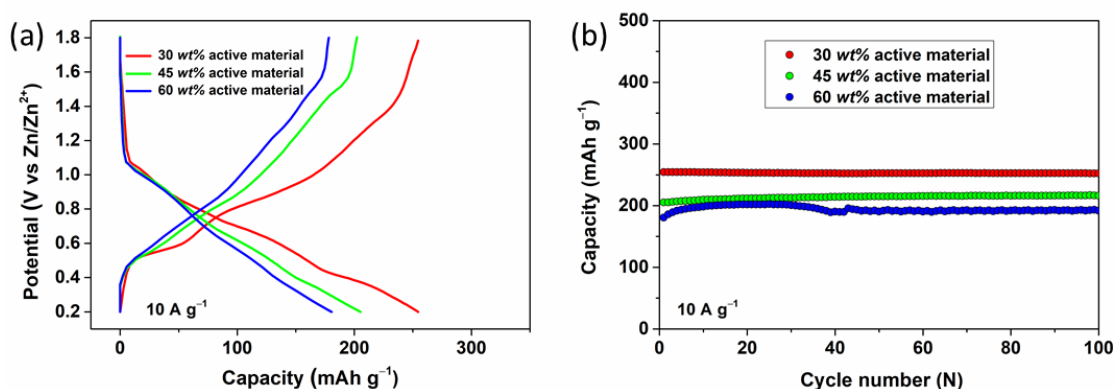


Fig. S10 (a) Discharge/charge profiles and (b) capacity retention plots of HATAQ electrodes with different amounts of active material at 10 A g⁻¹ (PVDF was kept constant at 10 wt%).

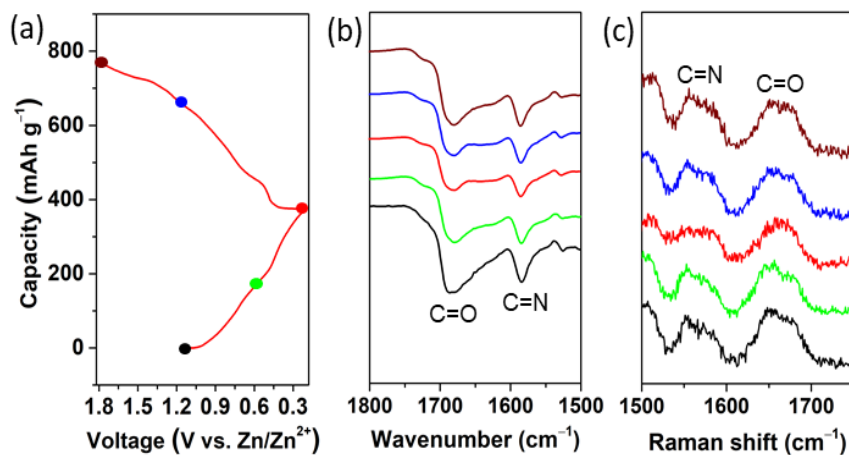


Fig. S11 (a) Discharge/charge profile at 200 mA g⁻¹ indicating the voltage positions for ex-situ experiments in 1 M ZnSO₄ aqueous electrolyte. (b) FT-IR spectra of the HATAQ electrodes at different charge/discharge states showing the change in intensity of C=O and C=N signals. (c) Ex-situ Raman spectra of HATAQ at corresponding voltage positions.

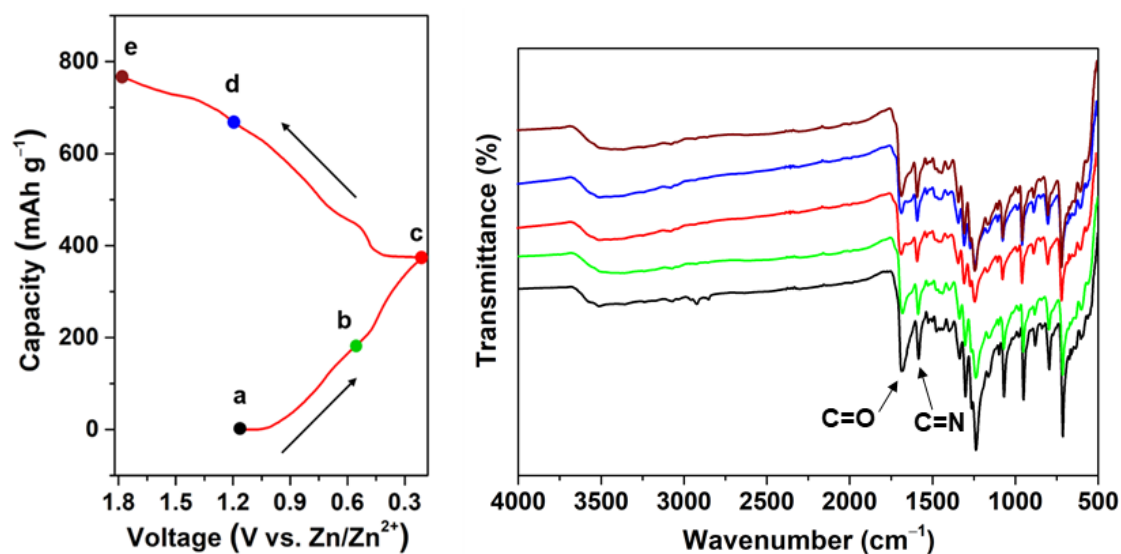


Fig. S12 Ex-situ FT-IR spectra of the HATAQ electrodes at different charge/discharge states at 200 mA g⁻¹ (wavenumber of 500–4000 cm⁻¹).

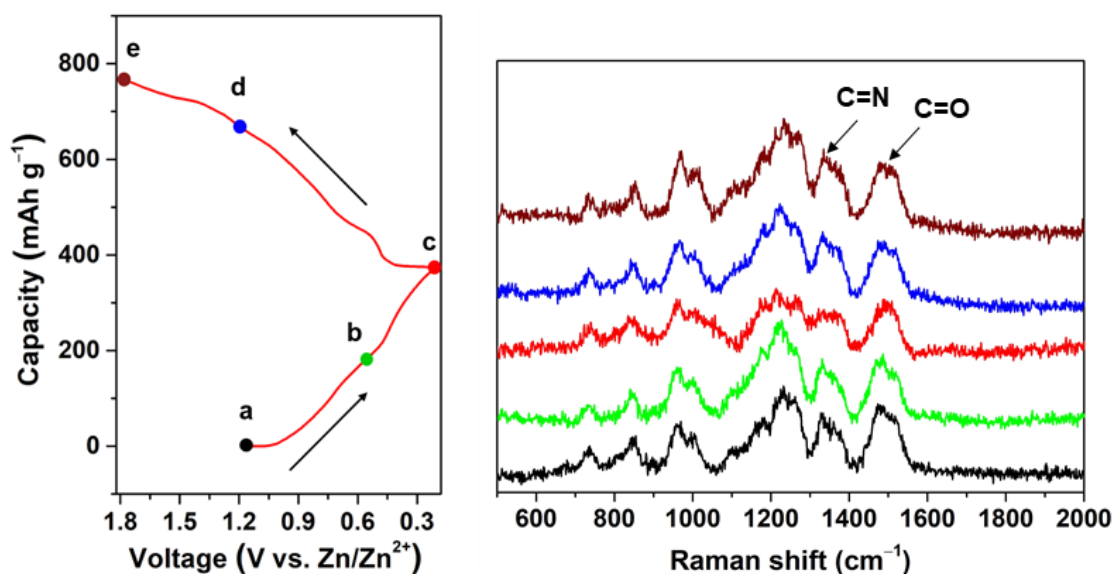


Fig. S13 Ex-situ Raman spectra of the HATAQ electrodes at different charge/discharge states at 200 mA g⁻¹ in the range of 500–2000 cm⁻¹.

Figure S11 and S12 show the FT-IR spectra at different discharge and charge states when HATAQ electrode was cycled at 200 mA g⁻¹. The distinct absorption peaks at 1687 and 1582 cm⁻¹ can be attributed to stretching vibration modes of carbonyl (C=O) and imine (C=N) groups, respectively.^{24,25} As the cell is discharged from open circuit voltage (OCV) to 0.2 V, the intensities of these two peaks gradually decrease, suggesting the interactions between the charged species in the electrolyte and both the carbonyl and imine redox centers in HATAQ during the reduction.^{1,26,27} At the fully charged state at 1.8 V, the intensities of the two peaks increase and become comparable to those at the pristine state, indicating the reversibility of the redox processes at the C=O and C=N groups. Similarly, the bands observed in the Raman spectra (Figure S11 and S13) at approximately 1570 and 1665 cm⁻¹ correspond to C=N and C=O, respectively.^{1,24,28} Both of the bands become weaker during discharge and stronger during charge. These results confirm the highly reversible nature of the redox processes in HATAQ as seen in the electrochemical tests. According to these results, it is clear that both carbonyl and imine groups of HATAQ are redox-active and both groups can interact with the guest species during discharge/charge processes. This may be explained by the very small difference in the atomic charges and electronegativity between O and N atoms in the extended π -conjugated HATAQ structure.

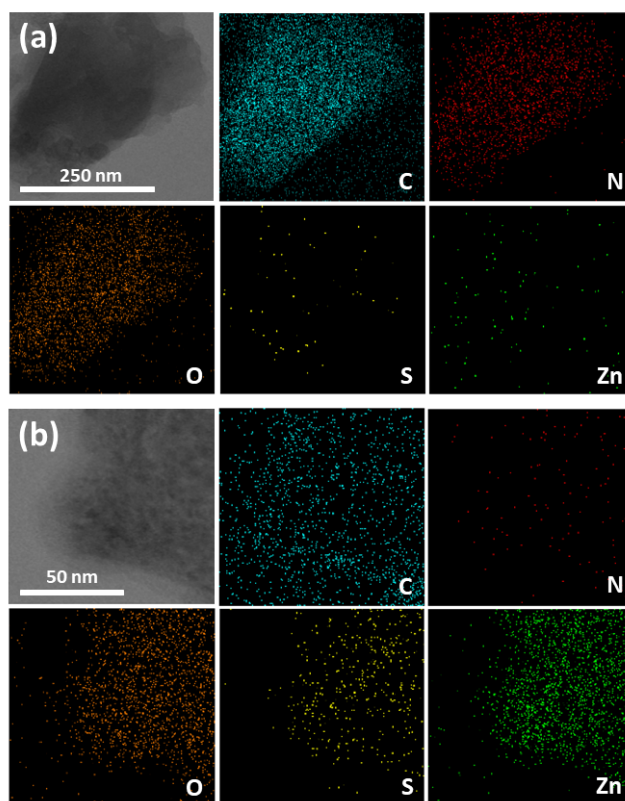


Fig. S14 STEM images with EDS mapping of (a) pristine HATAQ and (b) HATAQ discharged to 0.2 V at the rate of 200 mA g⁻¹ (unwashed with acetic acid), respectively, which show uniform distribution of C, N, and O of pristine HATAQ and uniform dispersion of O, S, and Zn confirming the presence of ZHS on discharged HATAQ surface.

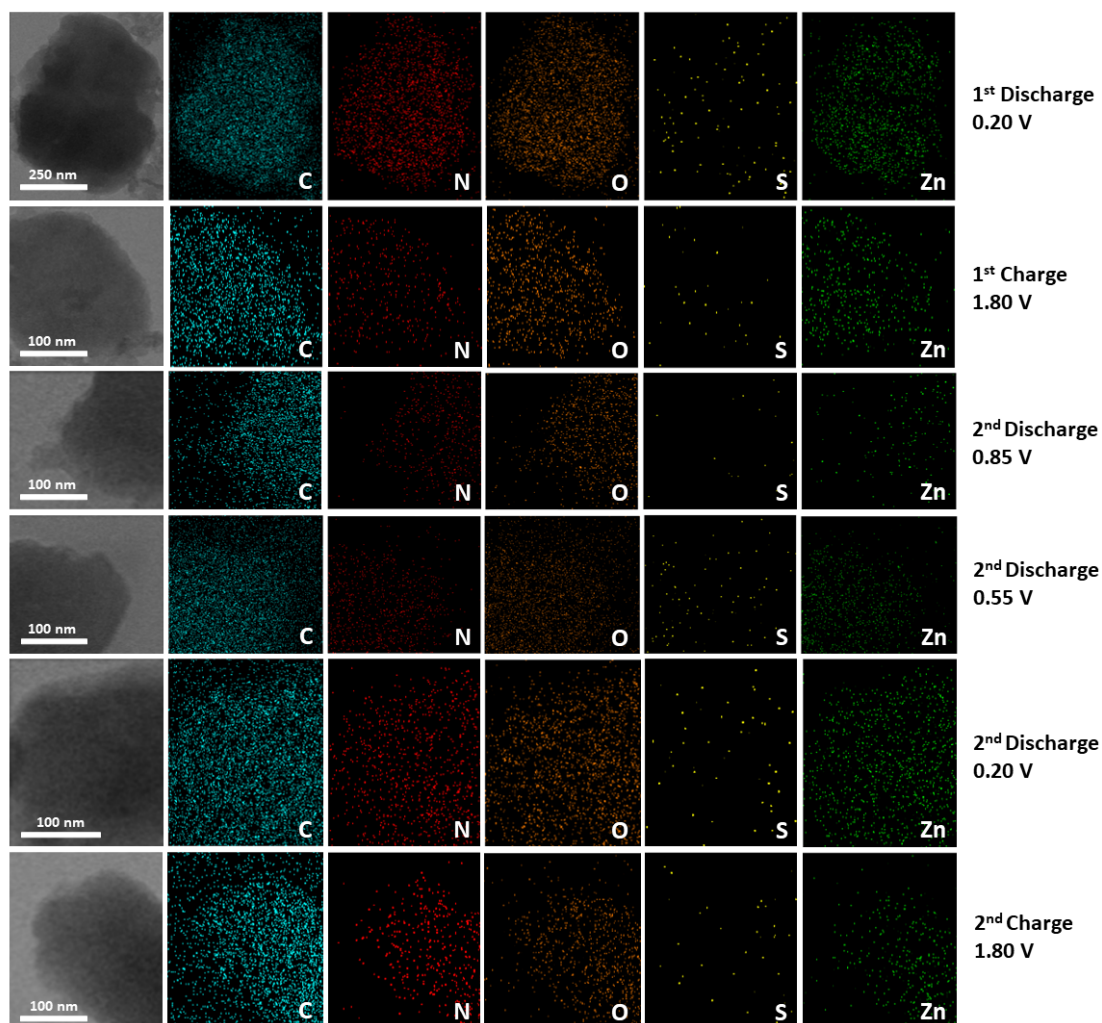


Fig. S15 STEM images with EDS mapping of HATAQ electrodes cycled at 200 mA g^{-1} that were washed with acetic acid for 10 s at different states of charge for 1st and 2nd cycle. The elemental mappings show uniform distribution of C, N, O, and Zn on the whole particle of HATAQ. Zn concentration appears to increase as discharge progresses and decrease during charge, which suggests some degree of interactions between Zn species and the cathode material at this low rate.

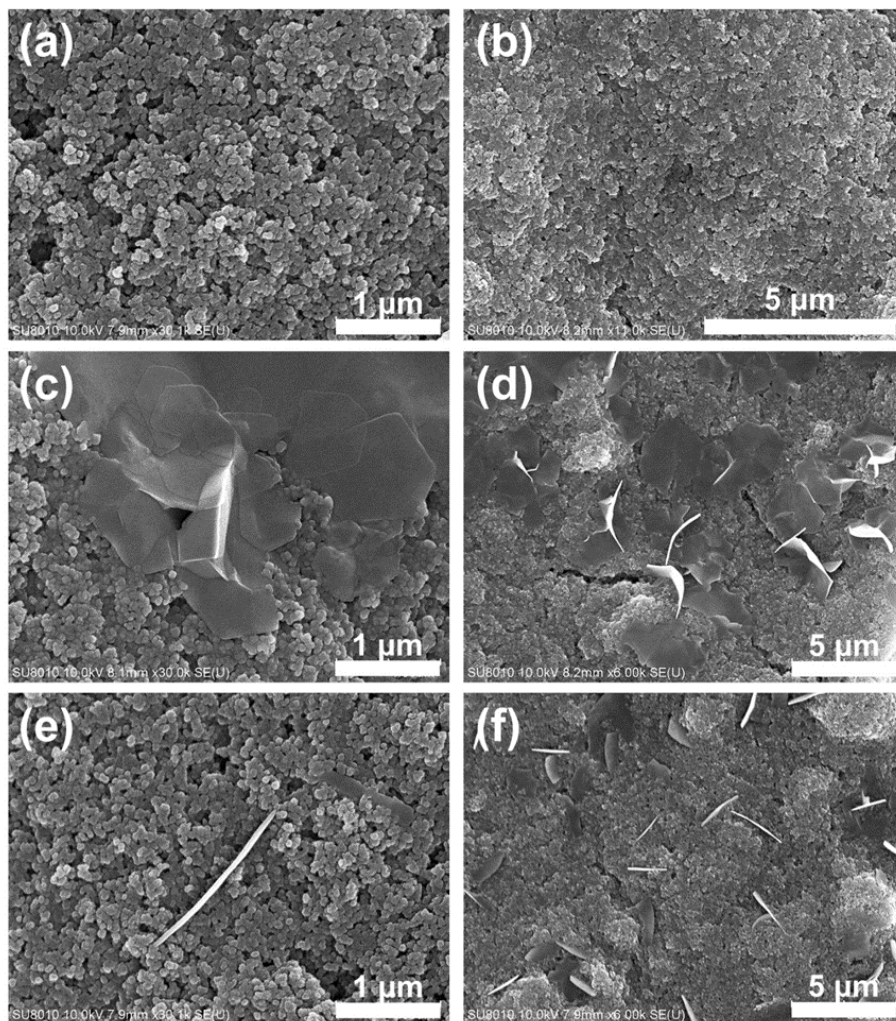


Fig. S16 SEM images of HATAQ electrodes at different magnifications: (a) and (b) pristine electrode; (c) and (d) at the end of discharge (0.2 V); (e) and (f) at the end of charge (1.8 V) cycled at the rate of 200 mA g⁻¹, revealing that the amount of ZHS on the electrode surface is significantly decreased during charge.

Ex-situ PXRD was carried out on electrodes at different voltage positions during discharge/charge processes (Figure 3c, main text). When the patterns from pristine electrode (dry) and electrode soaked in the electrolyte (wet) are compared with those discharged or charged, it is obvious that there is a new phase forming during discharge (indicated by *).^{29,30} The new peaks gradually become stronger during discharge and weaker during charge, which corresponds to the reversible formation of ZHS, Zn₄(OH)₆SO₄·xH₂O (where x = 0, 0.5, 1, 3, 4, and 5), described as a layered structure composed of stacked Zn(OH)₂ sheets with the interlayer spacing filled with ZnSO₄ and H₂O molecules.³¹⁻³³ The largest peak at ~12.4° confirms the presence of Zn₄(OH)₆SO₄·0.5 H₂O (JCPDS No. 44-0674), while the peaks at ~16.3° and 24.4° also suggest the co-existence of Zn₄(OH)₆SO₄·5H₂O (JCPDS No. 78-0246), as shown in

Table S1.³⁴ It is quite challenging to clearly indicate the exact nature due to the broad peaks observed in the PXRD data. However, it is worth noting that this phase transition from $\text{Zn}_4(\text{OH})_6\text{SO}_4 \cdot 5\text{H}_2\text{O}$ to $\text{Zn}_4(\text{OH})_6\text{SO}_4 \cdot 0.5\text{H}_2\text{O}$ is known to take place during the drying process of ex-situ electrodes after being disassembled. This loss of water molecules from the interlayer space has been reported previously.^{31-33,35}

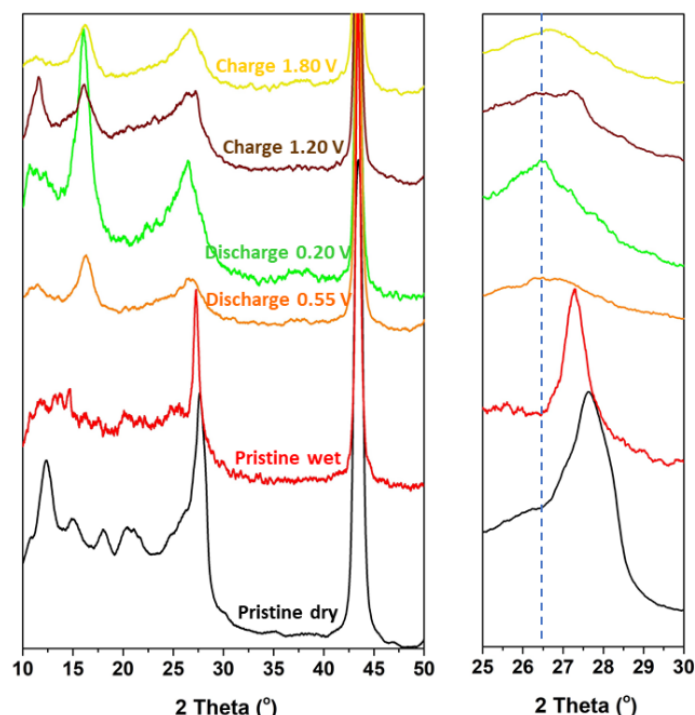


Fig. S17 Ex-situ PXRD patterns of HATAQ electrodes at different discharge/charge states compared to those at pristine conditions. The electrodes were washed with acetic acid for 10 s. (1 M ZnSO_4 aqueous electrolyte; 200 mA g^{-1}). The peak at 44° is from the stainless-steel mesh current collector.

The ZHS precipitate has been reported to be removed from electrodes by washing with acetic acid.³¹ In order to investigate the nature of redox processes in Zn/HATAQ cells, the disassembled electrodes were soaked in acetic acid for 10 s. PXRD data were then collected on the electrodes at different discharge/charge states compared to those at pristine conditions. Figure S17 shows that the peaks from ZHS are no longer present. When the HATAQ electrode is discharged from OCV down to the cutoff voltage at 0.2 V, the peak at $\sim 27^\circ$ corresponding to diffraction from the (006) plane, which is the layer stacking direction of HATAQ 2D arrangement, slightly shifts to a lower angle and subsequently moves back to a higher angle during charge.¹ This may be explained by a small increase in the interlayer spacing of HATAQ structure due to insertion of charged species during discharge and a decrease of the interlayer distance due to extraction during charge. The peak at $\sim 27^\circ$ remains visible throughout cycling, suggesting that the

HATAQ is still crystalline with π -stacking being intact and that the 2D layered structure is stable likely due to the in-plane supramolecular interactions, thus enhancing the cycling stability of HATAQ cathode.¹

In 1 M ZnSO_4 aqueous solution which is mildly acidic (pH \sim 4.5), Zn^{2+} acts as a weak acid through acid hydrolysis: $\text{Zn}(\text{H}_2\text{O})_x^{2+} \rightleftharpoons \text{Zn}(\text{H}_2\text{O})_{x-1}(\text{OH})^+ + \text{H}^+$, where x is the number of hydrated water molecules, most commonly found to be 4, 5, and 6.³⁶⁻³⁸ In this equilibrium, Zn^{2+} is coordinated to the weakly dissociating base, while the free H^+ (with the concentration of 10^{-4} – 10^{-5} M at pH of 4–5) causes the solution to be mildly acidic.³⁶ Due to the small ionic radius and low mass, H^+ possesses exceptional ionic mobility and is well-known to serve as a major charge carrier in aqueous media.^{29,39} Dissociation of water can also supply additional H^+ for the redox process at the cathode, resulting in an increase in local pH level (due to OH^-) and immediately causing the precipitation of flake-like $\text{Zn}_4(\text{OH})_6\text{SO}_4 \cdot 5\text{H}_2\text{O}$ at the electrode surface.^{29,36,39} The large amount of the ZHS precipitate as seen in SEM images (Figure 3b, main text and S16) suggests that the source of H^+ is not limited by the mildly acidic solution which only contains $\sim 10^{-5}$ M of H^+ but also comes from the dissociation of water.^{36,39} The hydration shell of the Zn^{2+} which contains the weakly dissociation base can promote further dissociation of water, thus leading to unlimited supply of H^+ at the electrode surface.^{36,39} Therefore, the formation of ZHS confirmed by techniques such as PXRD/STEM-EDS/high-energy X-ray scattering on a discharged electrode can be used to indicate proton insertion.^{36,39} ZHS reversible formation as observed in Figure 3c, main text and S16 also functions as a pH buffer for the system.^{36,39}

HATAQ electrodes (cycled at 200 mA g^{-1}) washed with acetic acid were also analyzed by XPS as shown in Figure S18. The C 1s spectrum of the pristine HATAQ electrode can be deconvoluted into five peaks, centered approximately at 284.5, 285.2, 286.2, 287.8, and 290.5 eV which are assigned to C=C, C–C, C=N, C=O, and C–F, respectively.^{24,26,40} When the cell is discharged from OCV down to 0.85, 0.55, and finally the cutoff voltage at 0.2 V, the C=N and peaks become gradually weakened, while two new peaks C–N (285.4 eV) and C–O (286.0 eV) emerge and get larger.^{26,41} This indicates that there are interactions between the charged species from the electrolyte and the two redox-active functional groups of HATAQ, C=O and C=N. As the cell is charged back to 0.6, 1.2, and 1.8 V, the C–N and C–O peaks become much weaker, whereas the C=O and C=N appear stronger as the cell voltage increases.

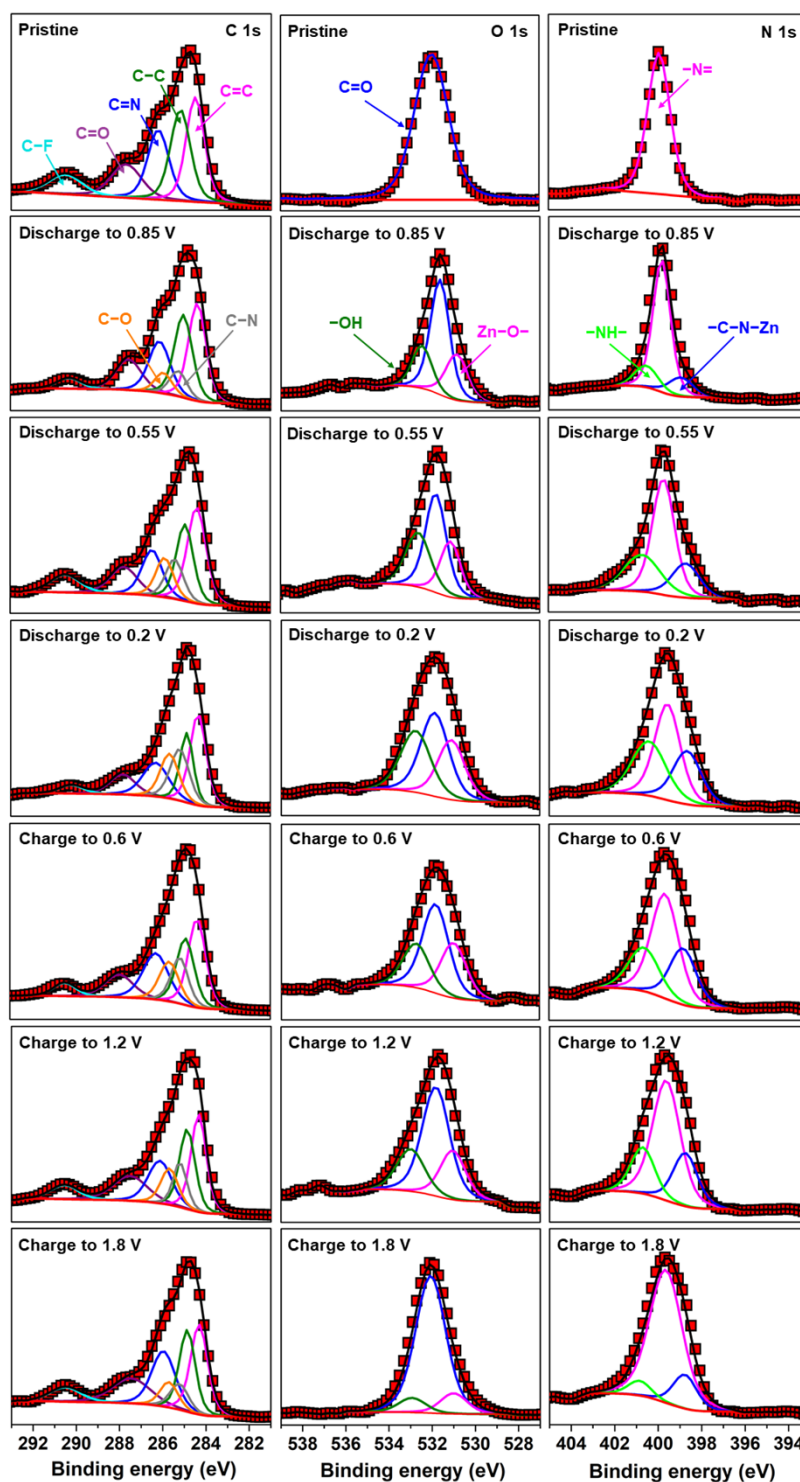


Fig. S18 Deconvolution of the high-resolution XPS spectra of HATAQ electrodes cycled at 200 mA g^{-1} that were washed with acetic acid for 10 s at different states of charge: (Left) C 1s; (Middle) O 1s; (Right) N 1s.

The O 1s and N 1s XPS spectra further reveal the nature of redox processes at the current density of 200 mA g^{-1} . The O 1s signal from the pristine electrode shows C=O peak (532.0 eV) which becomes smaller during discharge.^{38,42} As the electrode is

discharged to 0.85 V, two new peaks emerge at 530.85 and 532.5 eV corresponding to $-\text{Zn}-\text{O}$ and $-\text{OH}$, respectively, which become stronger as discharge continues.^{36,43,44} In case of N 1s, the pristine sample shows signal of $-\text{N}=$ at 399.9 eV.^{1,45} As the electrode is discharged, two peaks which can be attributed to $-\text{C}-\text{N}-\text{Zn}$ (398.9 eV) and $-\text{NH}-$ (400.5 eV) gradually emerge.^{36,39,46-48} During charge, these behaviors in both O 1s and N 1s spectra are found to be almost entirely reversible. The incomplete transformation may be in part due to the kinetic limitations in the solid-state electrochemical reaction.¹ These findings suggest interactions of both carbonyl and imine redox centers with H^+ (known for fast kinetics) and Zn species on the surface. It is worth noting that both STEM-EDS and XPS are surface characterization techniques; therefore, the fact that these results indicate a certain degree of coordination between the redox centers and Zn ions, which are commonly known to have much more sluggish transport kinetics compared to H^+ , is possible especially at such a low cycling rate of 200 mA g^{-1} .

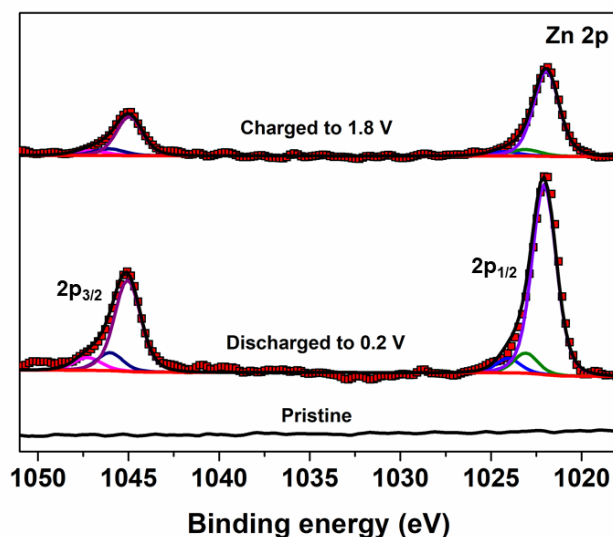


Fig. S19 Deconvolution of the high-resolution Zn 2p XPS spectra of HATAQ electrodes cycled at 200 mA g^{-1} that were washed with acetic acid for 10 s at the end of discharge and charge compared to pristine HATAQ.

Zn 2p XPS spectra (Figure S19) of discharged and charged electrodes show signals which can be convoluted into three pairs of Zn $2p_{1/2}$ and $2p_{3/2}$ peaks located at 1022.1/1045.1, 1023.1/1046.0, and 1024.1/1047.3, likely corresponding to Zn^{2+} coordinated to the surface of HATAQ and Zn^{2+} in $\text{Zn}(\text{OH})_2$ sheets and ZnSO_4 of ZHS, respectively.³⁰ At the end of charge, the amounts of both the surface coordinated Zn^{2+} and ZHS Zn^{2+} components appear to be lower than those at the end of discharge. These results indicate the removal of coordinated Zn^{2+} and that even after the washing of electrodes in acetic acid, a trace amount of ZHS phase is still present on electrode

surface. This may be contradicting to the PXRD results which show no peaks from ZHS. However, it is noteworthy that PXRD technique generally has a detection limit which needs to be met to order for the signal to be above the noise level. These findings suggest that sample handling and data analyzing should be done carefully to avoid misinterpretation especially for surface techniques. Zn signals may come from a residue of ZHS formed on electrode surface and are mistaken for Zn ions inserted to the bulk electrode.^{29,36,39,49}

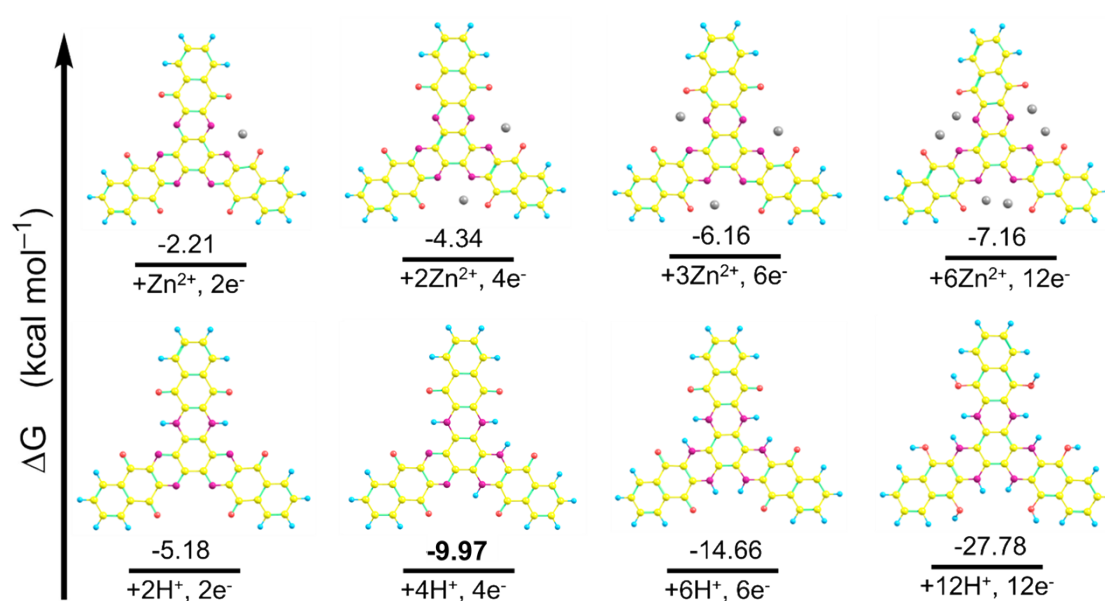


Fig. S20 Optimized (B3LYP/def2-SVP and the SMD solvation model) global minimum structures for the HATAQ-*n*H (*n* = 2,4,6,12) and HATAQ-*n*Zn (*n*= 1,2,3,6) complexes together with the corresponding Gibbs free energies (kcal mol⁻¹) for the complexation reaction between HATAQ and charge carriers (H⁺/Zn²⁺). The obtained results indicate strong thermodynamic preference for binding H⁺ vs. Zn²⁺. Color scheme: C, yellow; N, purple; O, red; Zn, metallic grey; H, blue.

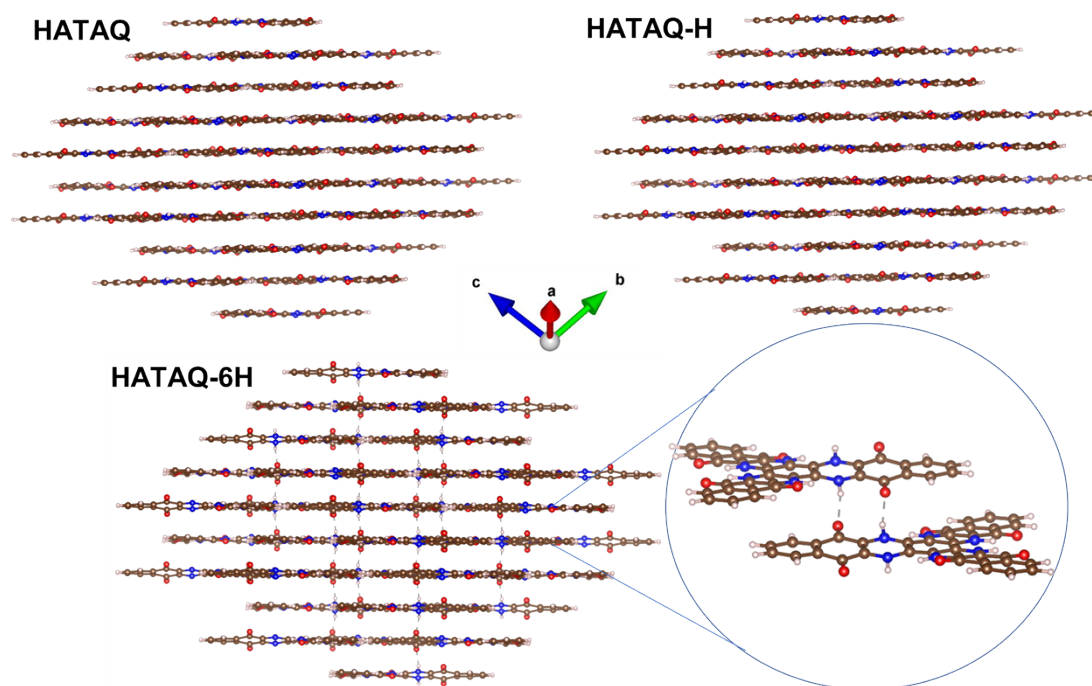


Fig. S21 Structural changes observed in the DFT optimized periodic HATAQ, HATAQ-H, and HATAQ-6H structures (the magnified region in HATAQ-6H shows the interlayer hydrogen bonds between -N-H and carbonyl oxygens). It can be seen that insertion of the first proton does not lead to the formation of the interlayer hydrogen bonds; instead, the C5 intramolecular hydrogen bond is formed accompanied by the appearance of the resonance-stabilized vinylogous amide group in HATAQ-H (Figure S23). When the structure reaches the maximum number of vinylogous amides in HATAQ-6H, during the DFT optimization we observed the formation of additional interlayer hydrogen bonds with the aromatic rings containing carbonyl and N-H groups slightly shifting out-of-plane to afford these hydrogen bond interactions. This would allow protons to travel within and across the HATAQ 2D layers.

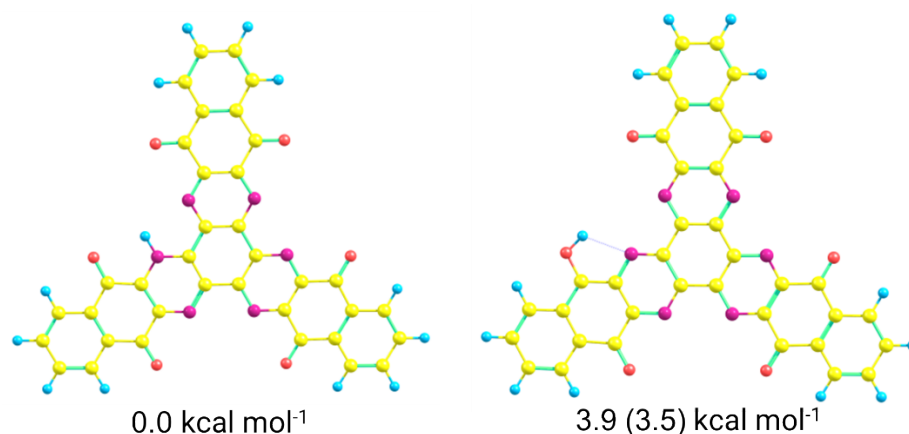


Fig. S22 Optimized structures and their relative Gibbs free energies (ZPE-corrected relative energies are given in parentheses) of the HATAQ-H molecule at the B3LYP/def2-SVP level of theory. ZPE = zero-point energy corrected. Color scheme: C, yellow; N, purple; O, red; H, blue.

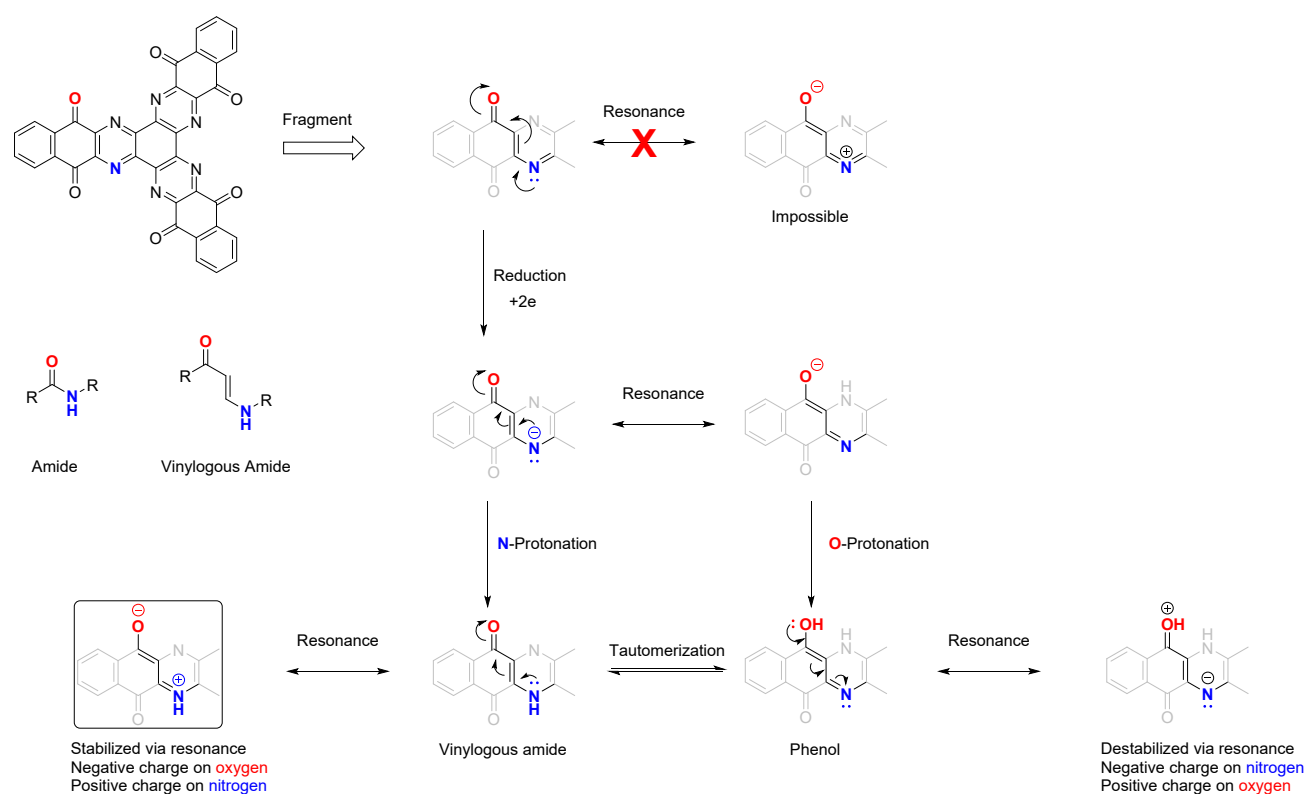


Fig. S23 Stabilization of N-protonated state over O –protonated state. Structure with N-protonated tautomer (vinyllogous amide) predicts increase in stabilization through resonance compared to the O-protonated tautomer.

Activation energy calculation

The activation energy for charge transfer (E_a) and ion diffusion (E_a') were calculated based on the Arrhenius equation (2) and (3), respectively.^{39,50}

$$\ln(R_{ct}^{-1}) = -E_a/RT + C \quad (2)$$

$$\ln(D) = -E_a'/RT + C' \quad (3)$$

where C and C' are constants, R is gas constant, and T is temperature. The charge transfer resistance (R_{ct}) was obtained by fitting Nyquist plots from EIS with a typical equivalent circuit (Figure S25). Diffusion coefficient (D) was calculated from GITT based on the following equation:^{39,51}

$$D = \frac{4L^2}{\pi\tau} \left(\frac{\Delta E_s}{\Delta E_t} \right)^2 \quad (4)$$

Where L is the diffusion length measured by the geometric thickness of cathode. τ is the relaxation time, ΔE_s is the steady-state voltage change, due to the current pulse and ΔE_t is the voltage change during the constant current pulse.

To gain insight into the charge transfer process in HATAQ, several electrochemical techniques were also used. EIS measurements were performed at different temperatures, 35, 40, 45, and 50 °C. The charge transfer resistance (R_{ct}) values were obtained by fitting the Nyquist plots using a typical equivalent circuit.^{39,50} The linear relationship between $\ln(R_{ct}^{-1})$ and T^{-1} shown in Figure S24 indicates the applicability of Arrhenius equation, $\ln(R_{ct}^{-1}) = -E_a/RT + C$. The activation energy E_a obtained from the plot is equal to 325 meV, which is considered small, therefore suggesting a facile ion desolvation process at the surface of HATAQ electrode.^{39,52,53} GITT was also carried out at various temperatures to investigate the proton conduction in HATAQ (Figure S25). The activation energy for ion diffusion can be calculated from the diffusion coefficient (D) values obtained from GITT as a function of temperature, according to the Arrhenius equation $\ln(D) = -E_a'/RT + C'$.^{39,51} The linear relationship between $\ln(D)$ and T^{-1} gives a low E_a' of 336 meV. This agrees well with our experimental and simulation results which support the unique proton conduction process via the Grotthuss mechanism (activation energy reported to be below 400 meV),^{39,50,54} where the proton transfer takes place by forming and breaking of hydrogen bonds between adjacent redox-active function groups, carbonyl and imine, in HATAQ. This will allow highly facile transport of ions compared to conventional ion diffusion process.³⁹

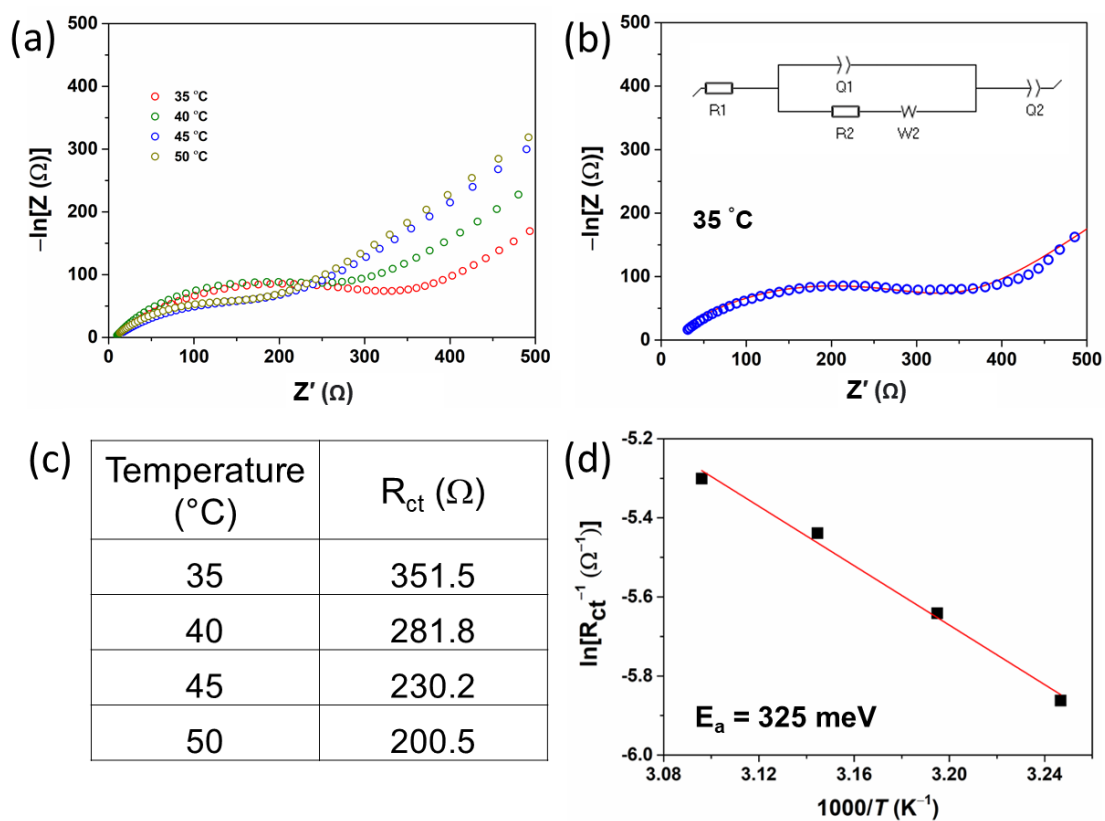


Fig. S24 EIS analysis of HATAQ electrodes used for determining E_a of charge transfer at electrode surface (1 M $ZnSO_4$ aqueous electrolyte): (a) Nyquist plots at various temperatures; (b) representative fitting of the Nyquist plot at 35 °C; (c) calculated R_{ct} at the temperatures analyzed; (d) Arrhenius plot of $\ln(R_{ct}^{-1})$ vs $1000(T^{-1})$.

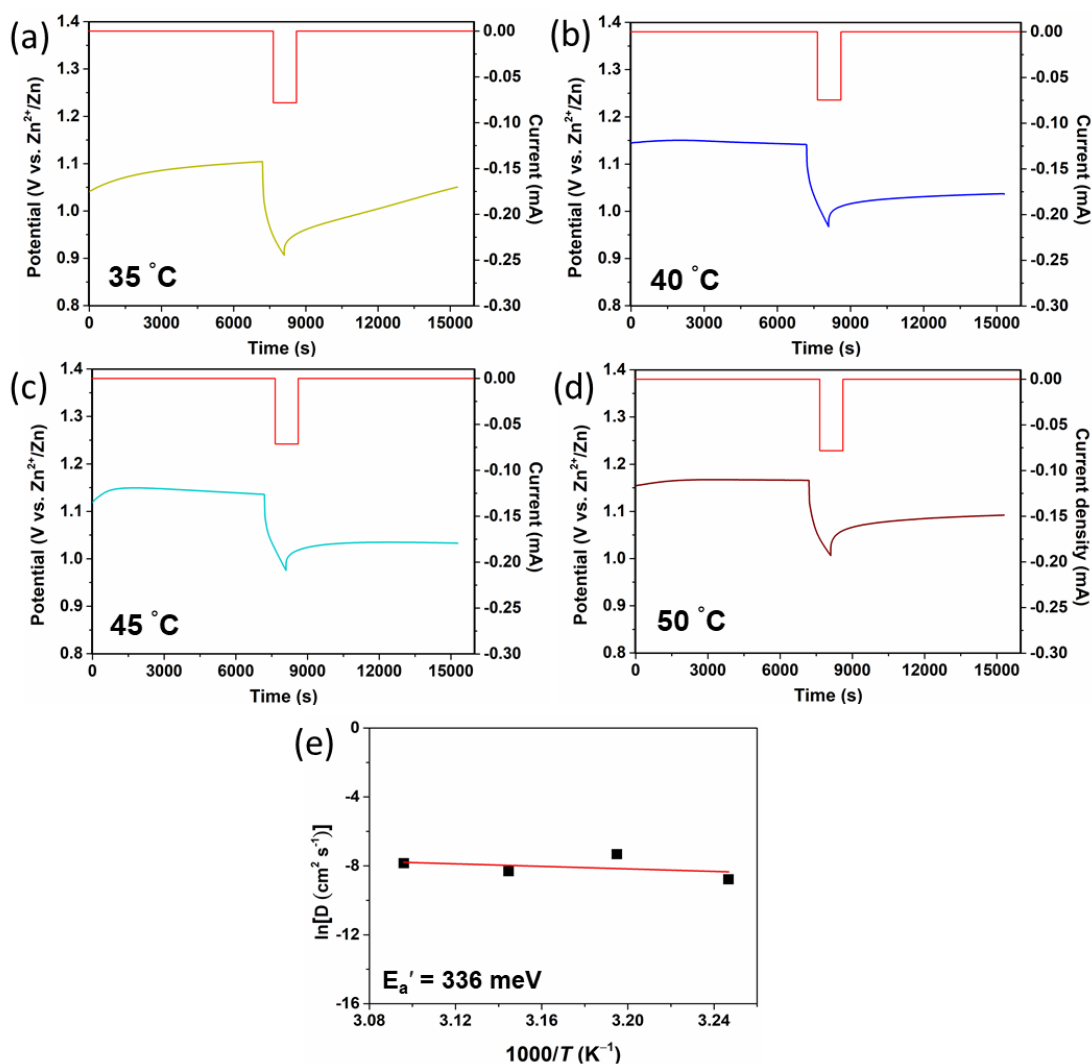


Fig. S25 (a) to (d) GITT curves of HATAQ electrodes (1 M ZnSO₄ aqueous electrolyte) at various temperatures used for determining E_a' of ion diffusion; (e) Arrhenius plot of $\ln(D)$ vs $1000(T^{-1})$.

Kinetic analysis (CV)

The discharge/charge kinetics of HATAQ was investigated by analyzing the CV data at various scan rates according to:

$$i = a\nu^b \quad (5)$$

$$i = k_1\nu + k_2\nu^{1/2} \quad (6)$$

where i is current at a fixed potential at the corresponding scan rate ν . Both a and b are coefficients in equation (5). The b values can be determined from the slope of $\log(i)$ vs $\log(\nu)$. In equation (6), $k_1\nu$ and $k_2\nu^{1/2}$ represent the surface capacitive current and diffusion-controlled current at specific potentials, respectively. k_1 and k_2 can be obtained by plotting $\nu^{1/2}$ vs $i/\nu^{1/2}$.^{50,54,55}

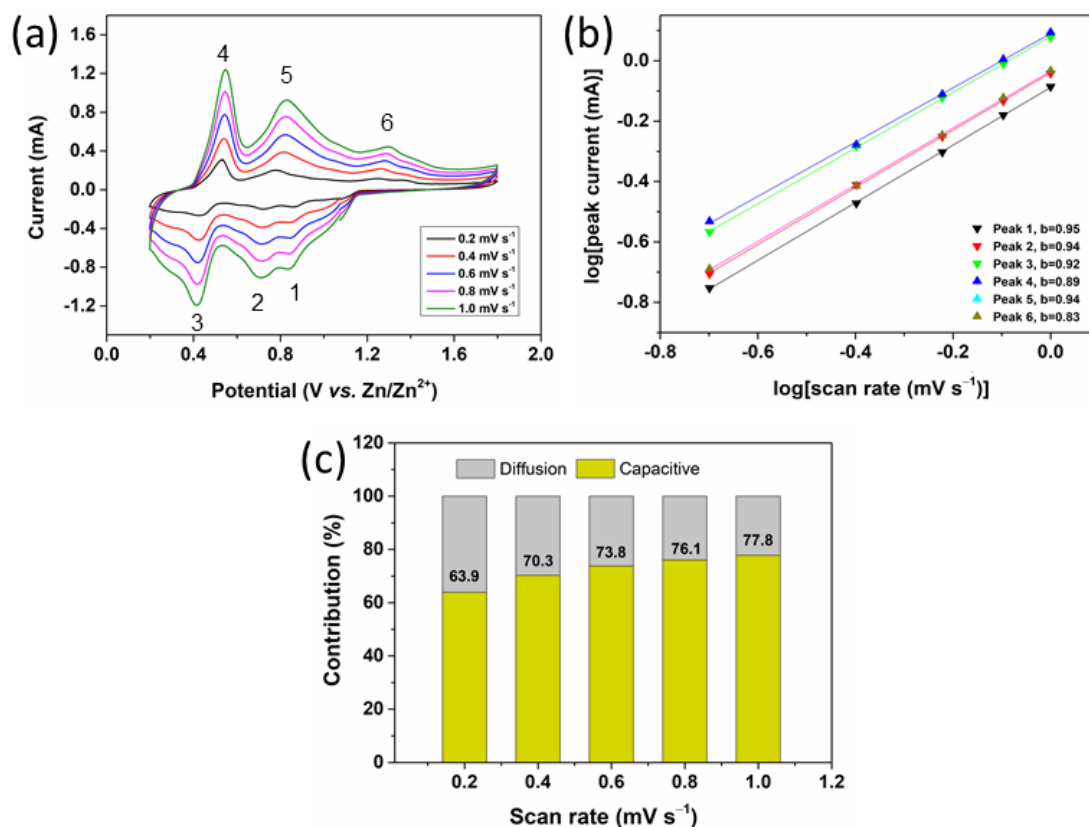


Fig. S26 (a) CV curves of HATAQ electrode at different scan rates in 1 M ZnSO₄ aqueous electrolyte. (b) Corresponding plots of $\log(i, \text{peak current})$ vs $\log(v, \text{scan rate})$ of the CV peaks according to equation (5). (c) Capacity contributions at different scan rates calculated according to equation (6).

CV was also used to further investigate the nature of charge storage processes during discharge/charge in HATAQ. The CV plots at different scan rates from 0.2 to 1.0 mV s⁻¹ are shown in Figure S26. The measured current i is fit to a power law relationship $i = av^b$ with scan rate v , and b is determined from the slope of the $\log(i)$ vs. $\log(v)$.^{50,54} The b values of all the redox peaks shown in Figure S26b are found to be close to 1, indicating the domination of non-diffusion-controlled charge storage process and facile redox kinetics of HATAQ.^{39,50,54} To further quantitatively differentiate the contributions of the capacitive and diffusion-controlled elements to the overall capacity, the relationship $i = av^b$ can be divided into two terms: the capacitive effects (k_1v) and diffusion-limited effects ($k_2v^{1/2}$) as follows: $i = k_1v + k_2v^{1/2}$, where i is the current (A) at a fixed potential.⁵⁴ By plotting $v^{1/2}$ vs $i/v^{1/2}$, k_1 and k_2 are derived from the slope and the y-axis intercept, respectively.^{39,54} As shown in Figure S26c, the ratio of stored charge contributed by capacitive process increases with the scan rate. Unlike the bulk diffusion-controlled process, a higher proportion of capacitive contribution at all the scan rates suggests an excellent rate performance of HATAQ cathode.⁵⁶

Energy density and power density calculation

The energy density of the HATAQ can be simplified as:^{57,58}

$$E_{electrode} = C \times V_{average} \quad (7)$$

Where $E_{electrode}$ is energy density (Wh kg^{-1}); C is the maximum delivered capacity (mAh g^{-1}); $V_{average}$ is the average operating voltage (C and $V_{average}$ can be obtained from the electrochemical measurements of HATAQ).

The power density of HATAQ at a specific rate can be estimated as:^{57,58}

$$P_{electrode} = \frac{E_{electrode}}{t} \quad (8)$$

Where $P_{electrode}$ is power density (W kg^{-1}); t is the discharge time (h).

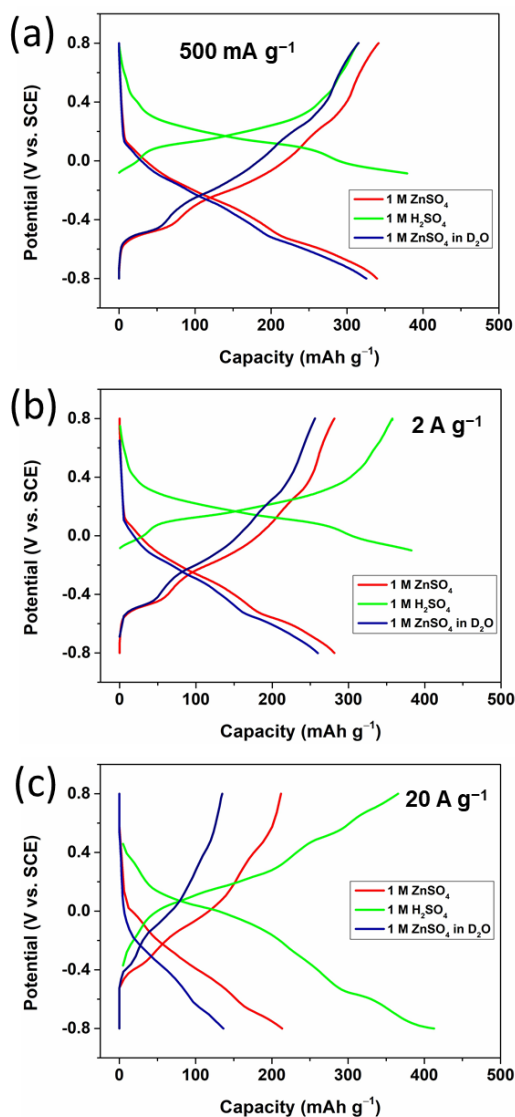


Fig. S27 Discharge/charge profiles of HATAQ from three-electrode cells with SCE reference electrode in different electrolyte systems, 1 M ZnSO₄ in H₂O (pH ~4.5), 1 M H₂SO₄ in H₂O (pH ~0), and 1 M ZnSO₄ in D₂O. (a) 500 mA g⁻¹; (b) 2 A g⁻¹; and (c) 20 A g⁻¹.

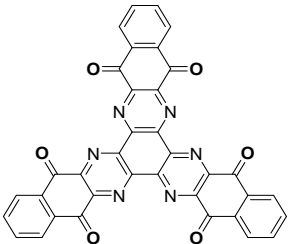
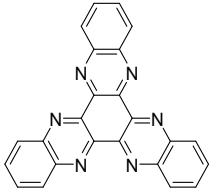
The domination of proton insertion in HATAQ was further verified by investigating the electrochemical behavior in various electrolyte systems using three-electrode cells with saturated calomel reference electrode (SCE) at different cycling rates, 500 mA g⁻¹, 2 A g⁻¹, and 20 A g⁻¹. The three electrolytes are 1 M ZnSO₄ in H₂O (pH ~4.5) where both H⁺ and Zn²⁺ are present, 1 M H₂SO₄ in H₂O (pH ~0) with only H⁺, and 1 M ZnSO₄ in D₂O with no H⁺ present.³⁹ As shown in Figure S27a, at the rate of 500 mA g⁻¹, the capacity values from ZnSO₄/H₂O and ZnSO₄/D₂O systems are almost comparable to that of H₂SO₄. This reveals that at such low rate, the overall transport kinetics of different types of charged species has no effect on the discharge/charge capacity within this voltage window (converted to approximately 0.2–1.8 V vs Zn/Zn²⁺). However, at the rate of 2 A g⁻¹, only the H₂SO₄ system can maintain the same capacity of ~400 mAh g⁻¹, while the ZnSO₄/H₂O and ZnSO₄/D₂O cells only provide 282 and 260 mAh g⁻¹, respectively. Furthermore, at the highest rate of 20 A g⁻¹, the system with H₂SO₄ electrolyte can deliver ~400 mAh g⁻¹, whereas the capacity values from both ZnSO₄/H₂O and ZnSO₄/D₂O significantly decrease with ZnSO₄/D₂O being the lowest. This is due to the transport kinetics of Zn²⁺ in general which is much more sluggish compared to that of H⁺, thus leading to large polarization and a low capacity at such a high rate.³⁹ At pH = 0, H₂SO₄ electrolyte has an H⁺ concentration of 1 M, while 1 M ZnSO₄ (pH ~4.5) has ~10⁻⁵ M of H⁺ together with the unlimited supply of H⁺ at the electrode surface from dissociation of H₂O (promoted by the equilibrium of hydrated Zn²⁺ species) accompanied by the precipitation of ZHS.^{36,38,59} The electrochemical results from HATAQ in H₂SO₄ electrolyte system at the three rates indicate that with such high concentration of H⁺ in the electrolyte, H⁺ can be supplied to the electrode surface to interact with HATAQ redox centers instantly; as a result, at an extremely high rate of 20 A g⁻¹, the capacity the same as that at low rate (500 mA g⁻¹) still can be obtained. This implies extraordinary transport kinetics of H⁺ both in the electrolyte and in HATAQ structure. In case of ZnSO₄/H₂O system, although it has unlimited supply of H⁺, the generation of additional H⁺ still relies on the dissociation of water and the formation of ZHS precipitate, which may not be as spontaneous.^{36,38,39} Therefore, we still can see the effect of rates on the capacity obtained. The results from ZnSO₄/D₂O system show that Zn-ion insertion has the poorest kinetics among all. Based on these observations, it is believed that in

ZnSO₄/H₂O electrolyte system, the contribution on the capacity obtained is still largely dominated by H⁺ insertion.

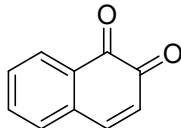
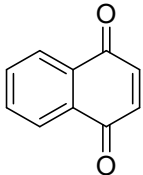
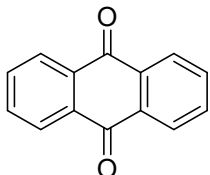
Table S1. Peak Lists of Zn₄(OH)₆SO₄·5H₂O and Zn₄(OH)₆SO₄·0.5H₂O from JCPDS Database.³⁴

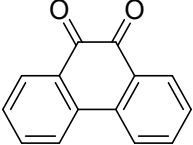
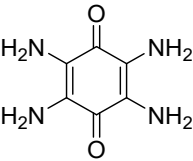
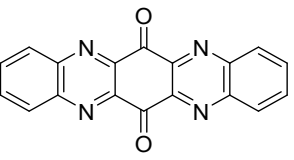
Zn ₄ (OH) ₆ SO ₄ ·5H ₂ O (JCPDS#78-0246)		Zn ₄ (OH) ₆ SO ₄ ·0.5H ₂ O (JCPDS#44-0674)	
2Theta [°]	Intensity [%]	2Theta [°]	Intensity [%]
8.093	100.0	12.352	100.0
16.277	5.0	17.340	7.0
24.444	3.0	25.136	91.0
32.947	3.2	32.717	55.0
35.422	3.2	35.122	80.0

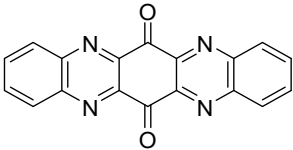
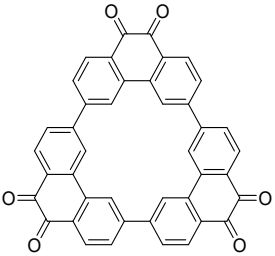
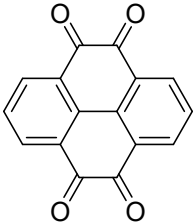
Table S2. Organic-based cathode materials for aqueous Zn-ion batteries reported in the literature (ED = energy density; PD = power density).

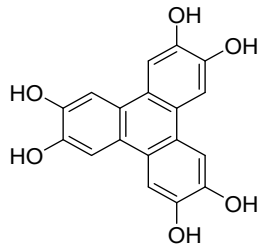
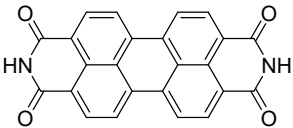
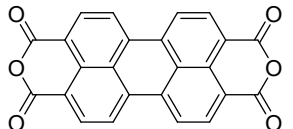
Compound	Electrode Composition (active material: conductive carbon: binder)	Electrolyte	Theoretical Capacity (Electron Transfer)	Voltage Window (V)	Initial Capacity at Lowest Rate Reported	Reversible Capacity at Highest Rate Reported	Capacity Retention at Highest Rate	Ref.
	HATAQ :Ketjen black (KB): polyvinylidene fluoride (PVDF) (3:6:1)	1 M aqueous ZnSO ₄	515 mAh g ⁻¹ (12 e ⁻)	0.2–1.8	492 mAh g ⁻¹ at 50 mA g ⁻¹	199 mAh g ⁻¹ at 20 A g ⁻¹	99 % after 1000 cycles (ED =344 Wh kg ⁻¹ at PD = 39 W kg ⁻¹ ED = 129 Wh kg ⁻¹ at PD = 13761 W kg ⁻¹)	This work and see also ref. [19] in the main text.
	HATN :Super P:PVDF (6:3.5:0.5)	2 M aqueous ZnSO ₄	418 mAh g ⁻¹ (6 e ⁻)	0.3–1.1	405 mAh g ⁻¹ at 100 mA g ⁻¹	140 mAh g ⁻¹ at 5 A g ⁻¹ (123 mAh g ⁻¹ at 20 A g ⁻¹ for 10 cycles)*	93.3 % after 5000 cycles at 5 A g ⁻¹	[29]

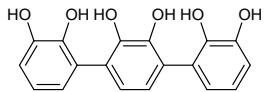
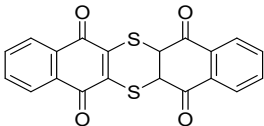
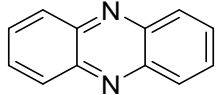
Compound	Electrode Composition (active material: conductive carbon: binder)	Electrolyte	Theoretical Capacity (Electron Transfer)	Voltage Window (V)	Initial Capacity at Lowest Rate Reported	Reversible Capacity at Highest Rate Reported	Capacity Retention at Highest Rate	Ref.
	DQP:KB: Polytetrafluoroethylene (PTFE) (6:3:1)	1 M aqueous ZnSO ₄	418 mAh g ⁻¹ (6 e ⁻)	0.2–1.4	413 mAh g ⁻¹ at 50 mA g ⁻¹	162 mAh g ⁻¹ at 5 A g ⁻¹	86 % after 1000 cycles (ED = 220 Wh kg ⁻¹ at PD = 25 W kg ⁻¹)	[49]
	HATN-3CN:KB:PVDF (6:3:1)	2 M aqueous ZnSO ₄	350 mAh g ⁻¹ (6 e ⁻)	0.1–1.6	320 mAh g ⁻¹ at 50 mA g ⁻¹	240 mAh g ⁻¹ at 5 A g ⁻¹ (~180 mAh g ⁻¹ at 20 A g ⁻¹ for 5 cycles)*	~90.7 % after 5800 cycles at 5 A g ⁻¹ (ED = 149. Wh kg ⁻¹ at PD = 24 W kg ⁻¹)	[59]
	C4Q:super P:PVDF (6:3.5:0.5)	3 M aqueous Zn(CF ₃ SO ₃) ₂	446 mAh g ⁻¹ (8 e ⁻)	0.2–1.8	335 mAh g ⁻¹ at 20 mA g ⁻¹	174 mAh g ⁻¹ at 500 mA g ⁻¹ (172 mAh g ⁻¹ at 1 A g ⁻¹ for 5 cycles)*	87 % after 1000 cycles at 500 mA g ⁻¹ (ED = 220 Wh kg ⁻¹ for pouch cell)	[60]

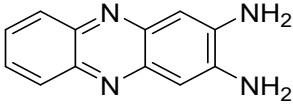
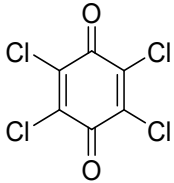
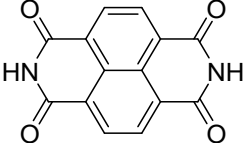
Compound	Electrode Composition (active material: conductive carbon: binder)	Electrolyte	Theoretical Capacity (Electron Transfer)	Voltage Window (V)	Initial Capacity at Lowest Rate Reported	Reversible Capacity at Highest Rate Reported	Capacity Retention at Highest Rate	Ref.
	1,2-NQ :super P:PVDF (6:3.5:0.5)	3 M aqueous Zn(CF ₃ SO ₃) ₂	339 mAh g ⁻¹ (2 e ⁻)	0.2–1.8	~69 mAh g ⁻¹ at 20 mA g ⁻¹	~51 mAh g ⁻¹ at 20 mA g ⁻¹	~74 % after 5 cycles at 20 mA g ⁻¹	[60]
	1,4-NQ :super P:PVDF (6:3.5:0.5)	3 M aqueous Zn(CF ₃ SO ₃) ₂	339 mAh g ⁻¹ (2 e ⁻)	0.2–1.8	~150 mAh g ⁻¹ at 20 mA g ⁻¹	~48 mAh g ⁻¹ at 20 mA g ⁻¹	~32 % after 5 cycles at 20 mA g ⁻¹	[60]
	9,10-AQ :super P:PVDF (6:3.5:0.5)	3 M aqueous Zn(CF ₃ SO ₃) ₂	258 mAh g ⁻¹ (2 e ⁻)	0.2–1.8	~195 mAh g ⁻¹ at 20 mA g ⁻¹	~125 mAh g ⁻¹ at 20 mA g ⁻¹	~64 % after 40 cycles at 20 mA g ⁻¹	[60]

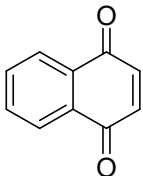
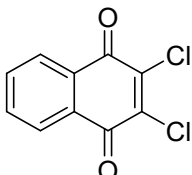
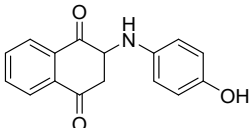
Compound	Electrode Composition (active material: conductive carbon: binder)	Electrolyte	Theoretical Capacity (Electron Transfer)	Voltage Window (V)	Initial Capacity at Lowest Rate Reported	Reversible Capacity at Highest Rate Reported	Capacity Retention at Highest Rate	Ref.
	9,10-PQ :super P:PVDF (6:3.5:0.5)	3 M aqueous Zn(CF ₃ SO ₃) ₂	258 mAh g ⁻¹ (2 e ⁻)	0.2–1.8	~111 mAh g ⁻¹ at 20 mA g ⁻¹	~88 mAh g ⁻¹ at 20 mA g ⁻¹	~79 % after 5 cycles at 20 mA g ⁻¹	[60]
	TABQ :KB:PVDF (5:4:1)	1 M aqueous ZnSO ₄	319 mAh g ⁻¹ (2 e ⁻)	0.4–1.3	303 mAh g ⁻¹ at 100 mA g ⁻¹	~240 mAh g ⁻¹ at 5 A g ⁻¹	~89 % after 1000 cycles at 5 A g ⁻¹	[39]
	TAPQ :KB:PTFE (6:3:1)	1 M aqueous ZnSO ₄	515 mAh g ⁻¹ (6 e ⁻)	0.1–1.6	443 mAh g ⁻¹ at 50 mA g ⁻¹	n/a (~20 mAh g ⁻¹ at 5 A g ⁻¹ for 10 cycles)*	68.7 % after 1000 cycles at 2 A g ⁻¹ (ED = 282 Wh kg ⁻¹)	[61]
				0.3–1.6	325 mAh g ⁻¹ at 50 mA g ⁻¹	n/a (~30 mAh g ⁻¹ at 5 A g ⁻¹ for 10 cycles)*	n/a	

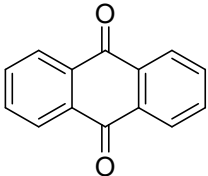
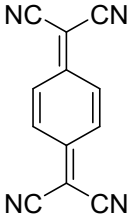
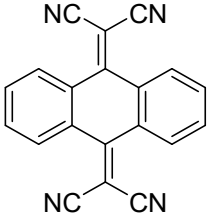
Compound	Electrode Composition (active material: conductive carbon: binder)	Electrolyte	Theoretical Capacity (Electron Transfer)	Voltage Window (V)	Initial Capacity at Lowest Rate Reported	Reversible Capacity at Highest Rate Reported	Capacity Retention at Highest Rate	Ref.
	TAPQ :KB:PTFE (6:3:1)	1 M aqueous ZnSO ₄	515 mAh g ⁻¹ (6 e ⁻)	0.5–1.6	270 mAh g ⁻¹ at 50 mA g ⁻¹	182 mAh g ⁻¹ at 2 A g ⁻¹ (~70 mAh g ⁻¹ at 5 A g ⁻¹ for 10 cycles)*	68.7 % after 1000 cycles at 2 A g ⁻¹ (ED = 227 Wh kg ⁻¹)	[61]
	PQ-Δ :AB:PVDF (6:3:1)	3 M aqueous Zn(CF ₃ SO ₃) ₂	216 mAh g ⁻¹ (2 e ⁻)	0.25–1.6	~200 mAh g ⁻¹ at 30 mA g ⁻¹	~200 mAh g ⁻¹ at 30 mA g ⁻¹	~100 % after 500 cycles	[42]
	PTO :KB:PTFE (3:6:1)	2 M aqueous ZnSO ₄	452 mAh g ⁻¹ (4 e ⁻)	0.36– 1.46	336 mAh g ⁻¹ at 40 mA g ⁻¹	145 mAh g ⁻¹ at 3 A g ⁻¹ (113 mAh g ⁻¹ at 20 A g ⁻¹ for 1 cycle)*	70 % after 1000 cycles at 3 A g ⁻¹ (ED = 186.7 Wh kg ⁻¹ at PD = 22.1 W kg ⁻¹)	[62]

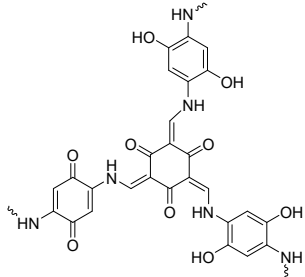
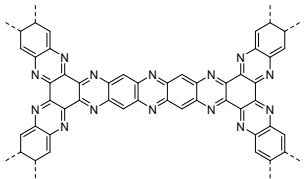
Compound	Electrode Composition (active material: conductive carbon: binder)	Electrolyte	Theoretical Capacity (Electron Transfer)	Voltage Window (V)	Initial Capacity at Lowest Rate Reported	Reversible Capacity at Highest Rate Reported	Capacity Retention at Highest Rate	Ref.
	HHTP :graphene oxide (GO):Super P:PTFE (2.3:4.7:2:1)	3 M aqueous ZnSO ₄	248 mAh g ⁻¹ (3 e ⁻)	0.2–1.5	223 mAh g ⁻¹ at 50 mA g ⁻¹	134 mAh g ⁻¹ at 10 A g ⁻¹	87.9 % after 7000 cycles (ED = 170 Wh kg ⁻¹ at PD = 40 W kg ⁻¹)	[63]
	PTCDI :rGO:PVDF (7:2:1)	3 M aqueous ZnSO ₄	135 mAh g ⁻¹ (2 e ⁻)	0.2–1.8	127 mAh g ⁻¹ at 50 mA g ⁻¹	130 mAh g ⁻¹ at 3 A g ⁻¹ (121 mAh g ⁻¹ at 5 A g ⁻¹ for 10 cycles)*	97 % after 1500 cycles (ED = 44 Wh kg ⁻¹)	[64]
	π-PCM :carbon black:PVDF (8:1:1)	2 M aqueous ZnCl ₂	136 mAh g ⁻¹ (2 e ⁻)	0.05–1.0	122.9 mAh g ⁻¹ at 200 mA g ⁻¹	~100 mAh g ⁻¹ at 8 A g ⁻¹ (76.9 mAh g ⁻¹ at 32 A g ⁻¹ for 1 cycles)*	68.2 % after 1000 cycles (PD = 14.8 kW kg ⁻¹)	[65]

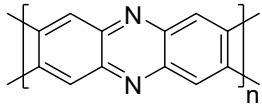
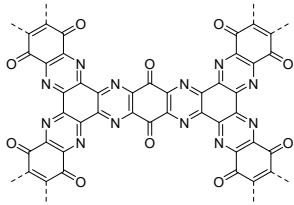
Compound	Electrode Composition (active material: conductive carbon: binder)	Electrolyte	Theoretical Capacity (Electron Transfer)	Voltage Window (V)	Initial Capacity at Lowest Rate Reported	Reversible Capacity at Highest Rate Reported	Capacity Retention at Highest Rate	Ref.
	PC/G-2 :acetylene black (AB):PVDF (7:2:1)	3 M aqueous ZnSO ₄	500 mAh g ⁻¹ (6 e ⁻)	0.2–1.9	355 mAh g ⁻¹ at 50 mA g ⁻¹	158 mAh g ⁻¹ at 1 A g ⁻¹ (~160 mAh g ⁻¹ at 5 A g ⁻¹ for 5 cycles)*	74.4 % after 3000 cycles at 1 A g ⁻¹	[66]
	DTT :KB:PTFE (6:3:1)	2 M aqueous ZnSO ₄	285 mAh g ⁻¹ (4 e ⁻)	0.3–1.4	211 mAh g ⁻¹ at 50 mA g ⁻¹	~78 mAh g ⁻¹ at 2 A g ⁻¹	83.3 % after 23000 cycles (ED = 127 Wh kg ⁻¹ at PD = 32 W kg ⁻¹)	[38]
	PNZ :KB:PTFE (6:3:1)	2 M aqueous ZnSO ₄	297 mAh g ⁻¹ (2 e ⁻)	0.45–1.7	232 mAh g ⁻¹ at 20 mA g ⁻¹	85 mAh g ⁻¹ at 1 A g ⁻¹	79 % after 1000 cycles (ED = 153 Wh kg ⁻¹ at PD = 44 W kg ⁻¹ ED = 70 Wh kg ⁻¹ at PD = 825 W kg ⁻¹)	[67]

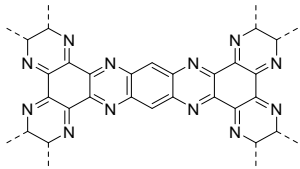
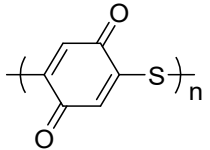
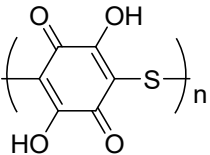
Compound	Electrode Composition (active material: conductive carbon: binder)	Electrolyte	Theoretical Capacity (Electron Transfer)	Voltage Window (V)	Initial Capacity at Lowest Rate Reported	Reversible Capacity at Highest Rate Reported	Capacity Retention at Highest Rate	Ref.
	DAP:KB:PTFE (6:3:1)	2 M aqueous ZnSO ₄	254 mAh g ⁻¹ (4 e ⁻)	0.45–1.7	213 mAh g ⁻¹ at 20 mA g ⁻¹	28 mAh g ⁻¹ at 100 mA g ⁻¹	29 % after 200 cycles	[67]
	TCB:CMK-3: carboxymethylcellulos (CMC) and styrene- butadiene rubber (SBR) (6:3.5:0.5)	1 M aqueous Zn(CF ₃ SO ₃) ₂	217 mAh g ⁻¹ (2 e ⁻)	0.8–1.4	~170 mAh g ⁻¹ at ~43 mA g ⁻¹	83 mAh g ⁻¹ at 217 mA g ⁻¹	70 % after 200 cycles	[68]
	NDI:super P:PVDF (6:3:1)	1 M aqueous ZnSO ₄	202 mAh g ⁻¹ (2 e ⁻)	0.2–1.0	~223 mAh g ⁻¹ at 202 mA g ⁻¹	~100 mAh g ⁻¹ at 202 mA g ⁻¹ (~25 mAh g ⁻¹ at 2020 mA g ⁻¹ for 5 cycles)*	44.8 % after 100 cycles at 202 mA g ⁻¹	[36]
				0.4–1.0	~123 mAh g ⁻¹ at 202 mA g ⁻¹	~100 mAh g ⁻¹ at 202 mA g ⁻¹ (~65 mAh g ⁻¹ at 2020 mA g ⁻¹ for 5 cycles)*	81.3 % after 1000 cycles at 202 mA g ⁻¹	

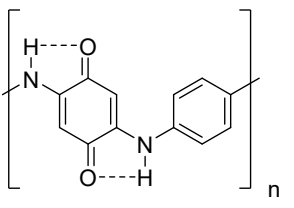
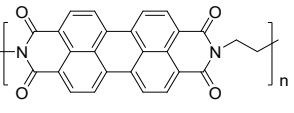
Compound	Electrode Composition (active material: conductive carbon: binder)	Electrolyte	Theoretical Capacity (Electron Transfer)	Voltage Window (V)	Initial Capacity at Lowest Rate Reported	Reversible Capacity at Highest Rate Reported	Capacity Retention at Highest Rate	Ref.
	NDQ :VGCF:PTFE (0.5:8.5:1.0)	2 M aqueous $\text{Zn}(\text{CF}_3\text{SO}_3)_2$	339 mAh g^{-1} ($2 e^-$)	0.1–1.65	333.5 mAh g^{-1} at 339 mA g^{-1}	137.2 mAh g^{-1} at 339 mA g^{-1} ($\sim 130 \text{ mAh g}^{-1}$ at 678 mA g^{-1} for 10 cycles)*	41 % after 1500 cycles	[69]
	Dichlone :VGCF:PTFE (0.5:8.5:1.0)	2 M aqueous $\text{Zn}(\text{CF}_3\text{SO}_3)_2$	336 mAh g^{-1} ($2 e^-$)	0.1–1.65	210.3 mAh g^{-1} at 236 mA g^{-1}	148.8 mAh g^{-1} at 236 mA g^{-1} (83.5 mAh g^{-1} at 2.36 A g^{-1} for 10 cycles)*	70.9 % after 1000 cycles	[69]
	BBQ :VGCF:PTFE (0.5:8.5:1.0)	2 M aqueous $\text{Zn}(\text{CF}_3\text{SO}_3)_2$	202 mAh g^{-1} ($4 e^-$)	0.1–1.65	202 mAh g^{-1} at 101 mA g^{-1}	136.9 mAh g^{-1} at 101 mA g^{-1} (160.3 mAh g^{-1} at 1.01 A g^{-1} for 10 cycles)*	~ 68 % after 1000 cycles	[69]

Compound	Electrode Composition (active material: conductive carbon: binder)	Electrolyte	Theoretical Capacity (Electron Transfer)	Voltage Window (V)	Initial Capacity at Lowest Rate Reported	Reversible Capacity at Highest Rate Reported	Capacity Retention at Highest Rate	Ref.
	AQ :super P:PTFE (6:3:1)	2 M aqueous ZnSO ₄	257 mAh g ⁻¹ (2 e ⁻)	0.2–1.2	188 mAh g ⁻¹ at 20 mA g ⁻¹	n/a	n/a (ED = 152 Wh kg ⁻¹ at PD = 46 W kg ⁻¹)	[70]
	TCNQ :super P:PTFE (6:3:1)	2 M aqueous ZnSO ₄	262 mAh g ⁻¹ (2 e ⁻)	0.6–1.8	192 mAh g ⁻¹ at 20 mA g ⁻¹	116 mAh g ⁻¹ at 100 mA g ⁻¹	65 % after 100 cycles at 100 mA g ⁻¹	[70]
	TCNAQ :super P:PTFE (6:3:1)	2 M aqueous ZnSO ₄	176 mAh g ⁻¹ (2 e ⁻)	0.6–1.8	169 mAh g ⁻¹ at 20 mA g ⁻¹	95 mAh g ⁻¹ at 500 mA g ⁻¹ (55 mAh g ⁻¹ at 1 A g ⁻¹ for 10 cycles)*	81 % after 1000 cycles at 500 mA g ⁻¹	[70]

Compound	Electrode Composition (active material: conductive carbon: binder)	Electrolyte	Theoretical Capacity (Electron Transfer)	Voltage Window (V)	Initial Capacity at Lowest Rate Reported	Reversible Capacity at Highest Rate Reported	Capacity Retention at Highest Rate	Ref.
	HqTp-COF :carbon nano fiber (CNF) (4:1)	3 M aqueous ZnSO ₄	442 mAh g ⁻¹ (24 e ⁻)	0.2–1.8	276 mAh g ⁻¹ at 125 mA g ⁻¹	81 mAh g ⁻¹ at 3.75 A g ⁻¹	95 % after 1000 cycles at 3.75 A g ⁻¹ (ED = 240 Wh kg ⁻¹ at PD = 109 W kg ⁻¹)	[71]
	PA-COF :AB:PTFE (6:3:1)	1 M aqueous ZnSO ₄	470 mAh g ⁻¹ (14 e ⁻ , calculated based on repetitive units)	0.2–1.6	247 mAh g ⁻¹ at 100 mA g ⁻¹	95 mAh g ⁻¹ at 1 A g ⁻¹ (68 mAh g ⁻¹ at 10 A g ⁻¹ for 5 cycles)*	62 % after 10000 cycles at 1 A g ⁻¹	[56]

	PoPD:AB:PVDF (7:2:1)	2 M aqueous ZnSO ₄	301 mAh g ⁻¹ (2 e ⁻)	0.25– 1.25	318 mAh g ⁻¹ at 50 mA g ⁻¹	104 mAh g ⁻¹ at 1 A g ⁻¹ (95 mAh g ⁻¹ at 5 A g ⁻¹ for 5 cycles)*	66.2 % after 3000 cycles at 1 A g ⁻¹	[48]
Compound	Electrode Composition (active material: conductive carbon: binder)	Electrolyte	Theoretical Capacity (Electron Transfer)	Voltage Window (V)	Initial Capacity at Lowest Rate Reported	Reversible Capacity at Highest Rate Reported	Capacity Retention at Highest Rate	Ref.
	HAQ-COF:AB:PTFE (6:3:1)	2 M aqueous ZnSO ₄	700 mAh g ⁻¹ (22 e ⁻ , calculated based on repetitive units)	0.2–1.6	344 mAh g ⁻¹ at 100 mA g ⁻¹	170 mAh g ⁻¹ at 5 A g ⁻¹ (96.5 mAh g ⁻¹ at 10 A g ⁻¹)	85 % after 10000 cycles at 5 A g ⁻¹	[72]

	HA-COF:AB:PTFE (6:3:1)	2 M aqueous ZnSO ₄	645 mAh g ⁻¹ (12 e ⁻ , calculated based on repetitive units)	0.2–1.6	164 mAh g ⁻¹ at 100 mA g ⁻¹	50.4 mAh g ⁻¹ at 5 A g ⁻¹ (35.4 mAh g ⁻¹ at 10 A g ⁻¹)	30 % after 10000 cycles at 5 A g ⁻¹	
	PBQS:n/a:PVDF (6:3:1)	3 M aqueous Zn(CF ₃ SO ₃) ₂	388 mAh g ⁻¹ (2 e ⁻)	0.2–1.8	203 mAh g ⁻¹ at 20 mA g ⁻¹	150 mAh g ⁻¹ at 40 mA g ⁻¹ (126 mAh g ⁻¹ at 1 A g ⁻¹ for 5 cycles)*	86 % after 50 cycles at 40 mA g ⁻¹ (ED = 193 Wh kg ⁻¹)	[73]
Compound	Electrode Composition (active material: conductive carbon: binder)	Electrolyte	Theoretical Capacity (Electron Transfer)	Voltage Window (V)	Initial Capacity at Lowest Rate Reported	Reversible Capacity at Highest Rate Reported	Capacity Retention at Highest Rate	Ref.
	PDBS:AB:PVDF (8:1:1)	2 M aqueous ZnSO ₄	268 mAh g ⁻¹ (2 e ⁻)	0.1–1.65	215 mAh g ⁻¹ at 50 mA g ⁻¹	197 mAh g ⁻¹ at 2 A g ⁻¹	~79 % after 2000 cycles (ED = 157 Wh kg ⁻¹ at PD = 31 W kg ⁻¹) ED = 2359 Wh kg ⁻¹ at PD = 75 W kg ⁻¹)	[74]

	PONEA:GO:PTFE (3:6:1)	3 M aqueous $\text{Zn}(\text{CF}_3\text{SO}_3)_2$	222 mAh g ⁻¹ (2 e ⁻)	0.2–1.6	329 mAh g ⁻¹ at 100 mA g ⁻¹	277 mAh g ⁻¹ at 10 A g ⁻¹ (270 mAh g ⁻¹ at 20 A g ⁻¹ for 5 cycles)*	85 % after 4800 cycles (ED = 242 Wh kg ⁻¹ at PD = 71 W kg ⁻¹ ED = 213 Wh kg ⁻¹ at PD = 15 W kg ⁻¹)	[75]
	PDI-EDA:n/a:PVDF (7.2:1.8:1.0)/ (8.1:0.9:1.0)	2 M aqueous ZnSO_4	120 mAh g ⁻¹ (2 e ⁻)	0.1–1.2	118 mAh g ⁻¹ at 50 mA g ⁻¹	98 mAh g ⁻¹ at 1 A g ⁻¹ (95 mAh g ⁻¹ at 5 A g ⁻¹ for 5 cycles)*	70.5 % after 1500 cycles at 1 A g ⁻¹	[76]

Note: * indicates capacity taken from the rate capability plot or the discharge/charge profile.

References

1. Wu, M. S.; Luu, N. T.; Chen, T. H.; Lyu, H.; Huang, T. W.; Dai, S.; Sun, X. G.; Ivanov, A. S.; Lee, J. C.; Popovs, I. Kaveevivitchai, W. Supramolecular self-assembled multi-electron-acceptor organic molecule as high-performance cathode material for Li-ion batteries. *Advanced Energy Materials* **2021**, *11*, 2170123.
2. Skinner, L. B.; Benmore, C. J.; Parise, J. B. Area detector corrections for high quality synchrotron X-ray structure factor measurements. *Nuclear Instruments and Methods in Physics Research Section A: Accelerators, Spectrometers, Detectors and Associated Equipment* **2012**, *662*, 61–70.
3. Ashiotis, G.; Deschildre, A.; Nawaz, Z.; Wright, J. P.; Karkoulis, D.; Picca, F. E.; Kieffer, J. The fast azimuthal integration Python library:pyFAI. *Journal of Applied Crystallography* **2015**, *48*, 510–519.
4. Wright CJ, Z. X. Computer-assisted area detector masking. *Journal of Synchrotron Radiation* **2017**, *24*, 506–508.
5. Qiu, X.; Thompson, J. W.; Billinge, S. J. PDFgetX2: a GUI-driven program to obtain the pair distribution function from X-ray powder diffraction data. *Journal of Applied Crystallography* **2004**, *37*, 678–678.
6. Egami, T. Egami; S. J. Billinge, *Underneath the Bragg Peaks: Structural Analysis of Complex Materials* **2012**, Newnes.
7. Fischer, H. E.; Barnes, A. C.; Salmon, P. S. Neutron and X-ray diffraction studies of liquids and glasses. *Reports on Progress in Physics* **2005**, *69*, 233.
8. Frisch, M. J.; Trucks, G. W.; Schlegel, H. B.; Scuseria, G. E.; Robb, M. A.; Cheeseman, J. R.; Scalmani, G.; Barone, V.; Petersson, G. A.; Nakatsuji, H.; Li, X.; Caricato, M.; Marenich, A. V.; Bloino, J.; Janesko, B. G.; Gomperts, R.; Mennucci, B.; Hratchian, H. P.; Ortiz, J. V.; Izmaylov, A. F.; Sonnenberg, J. L.; Williams; ; Ding, F.; Lipparini, F.; Egidi, F.; Goings, J.; Peng, B.; Petrone, A.; Henderson, T.; Ranasinghe, D.; Zakrzewski, V. G.; Gao, J.; Rega, N.; Zheng, G.; Liang, W.; Hada, M.; Ehara, M.; Toyota, K.; Fukuda, R.; Hasegawa, J.; Ishida, M.; Nakajima, T.; Honda, Y.; Kitao, O.; Nakai, H.; Vreven, T.; Throssell, K.; Montgomery, J. A., Jr.; Peralta, J. E.; Ogliaro, F.; Bearpark, M. J.; Heyd, J. J.; Brothers, E. N.; Kudin, K. N.; Staroverov, V. N.; Keith, T. A.; Kobayashi, R.; Normand, J.; Raghavachari, K.; Rendell, A. P.; Burant, J. C.; Iyengar, S. S.; Tomasi, J.; Cossi, M.; Millam, J. M.; Klene, M.; Adamo, C.; Cammi, R.; Ochterski, J. W.; Martin, R. L.; Morokuma, K.; Farkas, O.; Foresman, J. B.; Fox, D. J. Gaussian 16, Rev. A.03., Wallingford, CT, **2016**.
9. Marenich, A. V.; Cramer, C. J.; Truhlar, D. G. Universal solvation model based on solute electron density and on a continuum model of the solvent defined by the bulk dielectric constant and atomic surface tensions. *Journal of Physical Chemistry B* **2009**, *113*, 6378–6396.

10. Sergeeva, A. P.; Averkiev, B. B.; Zhai, H.J.; Boldyrev, A. I.; Wang, L.S. All-boron analogues of aromatic hydrocarbons: B17⁻ and B18⁻. *The Journal of Chemical Physics* **2011**, *134*, 224304.
11. Ivanov, A. S.; Morris, A. J.; Bozhenko, K. V.; Pickard, C. J.; Boldyrev, A. I. Inorganic double-helix structures of unusually simple lithium–phosphorus species. *Angewandte Chemie International Edition* **2012**, *51*, 8330–8333.
12. Glendening, E.D.; Landis, C. R.; Weinhold, F. NBO 6.0: Natural bond orbital analysis program. *Journal of Computational Chemistry* **2013**, *34*, 1429–1437.
13. Foster, J. P.; Weinhold, F. Natural hybrid orbitals. *Journal of the American Chemical Society* **1980**, *102*, 7211–7218.
14. Kresse, G.; Hafner, J. Ab initio molecular dynamics for liquid metals. *Physical Review B* **1993**, *47*, 558–561.
15. Kresse, G.; Hafner, J. Ab initio molecular-dynamics simulation of the liquid-metal–amorphous-semiconductor transition in germanium. *Physical Review B* **1994**, *49*, 14251–14269.
16. Kresse, G.; Furthmüller, J. Efficient iterative schemes for ab initio total-energy calculations using a plane-wave basis set. *Physical Review B* **1996**, *54*, 11169–11186.
17. Kresse, G.; Furthmüller, J. Efficiency of ab-initio total energy calculations for metals and semiconductors using a plane-wave basis set. *Computational Materials Science* **1996**, *6*, 15–50.
18. Blöchl, P. E. Projector augmented-wave method. *Physical Review B* **1994**, *50*, 17953–17979.
19. Kresse, G.; Joubert, D. From ultrasoft pseudopotentials to the projector augmented-wave method. *Physical Review B* **1999**, *59*, 1758–1775.
20. Perdew, J. P.; Burke, K.; Ernzerhof, M. Generalized gradient approximation made simple. *Physical Review Letters* **1996**, *77*, 3865–3868.
21. Grimme, S.; Antony, J.; Ehrlich, S.; Krieg, H. A consistent and accurate ab initio parametrization of density functional dispersion correction (DFT-D) for the 94 elements H-Pu. *Journal of Chemical Physics* **2010**, *132*, 154104.
22. Pulay, P. Convergence acceleration of iterative sequences. The case of SCF iteration. *Chemical Physics Letters* **1980**, *73*, 393–398.
23. Wu, S.; Wang, W.; Li, M.; Cao, L.; Lyu, F.; Yang, M.; Wang, Z.; Shi, Y.; Nan, B.; Yu, S.; Sun, Z.; Liu, Y.; Lu, Z. Highly durable organic electrode for sodium-ion batteries via a stabilized α -C radical intermediate. *Nature Communications* **2016**, *7*, 13318.
24. Lei, Z.; Yang, Q.; Xu, Y.; Guo, S.; Sun, W.; Liu, H.; Lv, L.-P.; Zhang, Y.; Wang, Y. Boosting lithium storage in covalent organic framework via activation of 14-electron redox chemistry. *Nature Communications* **2018**, *9*, 576.

25. Zhu, Y.; Chen, P.; Zhou, Y.; Nie, W.; Xu, Y. New family of organic anode without aromatics for energy storage. *Electrochimica Acta* **2019**, *318*, 262–271.
26. Shi, R.; Liu, L.; Lu, Y.; Wang, C.; Li, Y.; Li, L.; Yan, Z.; Chen, J. Nitrogen-rich covalent organic frameworks with multiple carbonyls for high-performance sodium batteries. *Nature Communications* **2020**, *11*, 178.
27. Lin, Z.-Q.; Xie, J.; Zhang, B.-W.; Li, J.-W.; Weng, J.; Song, R.-B.; Huang, X.; Zhang, H.; Li, H.; Liu, Y. Solution-processed nitrogen-rich graphene-like holey conjugated polymer for efficient lithium ion storage. *Nano Energy* **2017**, *41*, 117–127.
28. Zhuang, B.; Fujitsuka, M.; Tojo, S.; Cho, D. W.; Choi, J.; Majima, T. Influence of charge distribution on structural changes of aromatic imide derivatives upon one-electron reduction revealed by time-resolved resonance Raman spectroscopy during pulse radiolysis. *Journal of Physical Chemistry A* **2018**, *122*, 8738–8744.
29. Tie, Z.; Liu, L.; Deng, S.; Zhao, D.; Niu, Z. Proton insertion chemistry of a zinc–organic battery. *Angewandte Chemie International Edition* **2020**, *59*, 4920–4924.
30. Wan, F.; Zhang, L.; Dai, X.; Wang, X.; Niu, Z.; Chen, J. Aqueous rechargeable zinc/sodium vanadate batteries with enhanced performance from simultaneous insertion of dual carriers. *Nature Communications* **2018**, *9*, 1656.
31. Lee, B.; Seo, H. R.; Lee, H. R.; Yoon, C. S.; Kim, J. H.; Chung, K. Y.; Cho, B. W.; Oh, S. H. Critical role of pH evolution of electrolyte in the reaction mechanism for rechargeable zinc batteries. *ChemSusChem* **2016**, *9*, 2948–2956.
32. Bear, I. J.; Grey, I. E.; Newnham, I. E.; Rogers, L. J. The $\text{ZnSO}_4 \cdot 3\text{Zn}(\text{OH})_2 \cdot \text{H}_2\text{O}$ system. I. Phase formation. *Australian Journal of Chemistry* **1987**, *40*, 539–556.
33. Morin, S. A.; Forticaux, A.; Bierman, M. J.; Jin, S. Screw dislocation-driven growth of two-dimensional nanoplates. *Nano Letters* **2011**, *11*, 4449–4455.
34. Sambandam, B.; Soundharrajan, V.; Kim, S.; Alfaruqi, M. H.; Jo, J.; Kim, S.; Mathew, V.; Sun, Y.-k.; Kim, J., Aqueous rechargeable Zn-ion batteries: An imperishable and high-energy $\text{Zn}_2\text{V}_2\text{O}_7$ nanowire cathode through intercalation regulation. *Journal of Materials Chemistry A* **2018**, *6*, 3850–3856.
35. Moezzi, A.; Cortie, M. B.; McDonagh, A. M. Zinc hydroxide sulphate and its transformation to crystalline zinc oxide. *Dalton Transactions* **2013**, *42*, 14432–14437.
36. Na, M.; Oh, Y.; Byon, H. R. Effects of Zn^{2+} and H^+ association with naphthalene diimide electrodes for aqueous Zn-ion batteries. *Chemistry of Materials* **2020**, *32*, 6990–6997.
37. Hartmann, M.; Clark, T.; van Eldik, R. Hydration and water exchange of zinc (II) ions. Application of density functional theory. *Journal of the American Chemical Society* **1997**, *119*, 7843–7850.
38. Wang, Y.; Wang, C.; Ni, Z.; Gu, Y.; Wang, B.; Guo, Z.; Wang, Z.; Bin, D.; Ma, J.; Wang, Y. Binding zinc ions by carboxyl groups from adjacent molecules toward

- long-life aqueous zinc–organic batteries. *Advanced Materials* **2020**, *32*, 2000338.
39. Lin, Z.; Shi, H.-Y.; Lin, L.; Yang, X.; Wu, W.; Sun, X. A high capacity small molecule quinone cathode for rechargeable aqueous zinc-organic batteries. *Nature Communications* **2021**, *12*, 4424.
 40. Xue, Q.; Li, D.; Huang, Y.; Zhang, X.; Ye, Y.; Fan, E.; Li, L.; Wu, F.; Chen, R. Vitamin K as a high-performance organic anode material for rechargeable potassium ion batteries. *Journal of Materials Chemistry A* **2018**, *6*, 12559–12564.
 41. Guo, R.; Wang, Y.; Heng, S.; Zhu, G.; Battaglia, V. S.; Zheng, H. Pyromellitic dianhydride: A new organic anode of high electrochemical performances for lithium ion batteries. *Journal of Power Sources* **2019**, *436*, 226848.
 42. Nam, K. W.; Kim, H.; Beldjoudi, Y.; Kwon, T.-w.; Kim, D. J.; Stoddart, J. F. Redox-active phenanthrenequinone triangles in aqueous rechargeable zinc batteries. *Journal of the American Chemical Society* **2020**, *142*, 2541–2548.
 43. Ferraria, A. M.; da Silva, J. D. L.; do Rego, A. M. B. XPS studies of directly fluorinated HDPE: Problems and solutions. *Polymer* **2003**, *44*, 7241–7249.
 44. Oh, Y. J.; Yoo, J. J.; Kim, Y. I.; Yoon, J. K.; Yoon, H. N.; Kim, J.-H.; Park, S. B. Oxygen functional groups and electrochemical capacitive behavior of incompletely reduced graphene oxides as a thin-film electrode of supercapacitor. *Electrochimica Acta* **2014**, *116*, 118–128.
 45. Man, Z.; Li, P.; Zhou, D.; Zang, R.; Wang, S.; Li, P.; Liu, S.; Li, X.; Wu, Y.; Liang, X. High-performance lithium–organic batteries by achieving 16 lithium storage in poly (imine-anthraquinone). *Journal of Materials Chemistry A* **2019**, *7*, 2368–2375.
 46. Pan, D.; Wang, L.; Li, Z.; Geng, B.; Zhang, C.; Zhan, J.; Yin, L.; Wang, L. Synthesis of graphene quantum dot/metal–organic framework nanocomposites as yellow phosphors for white light-emitting diodes. *New Journal of Chemistry* **2018**, *42*, 5083–5089.
 47. Al-Gaashani, R.; Radiman, S.; Daud, A.; Tabet, N.; Al-Douri, Y. XPS and optical studies of different morphologies of ZnO nanostructures prepared by microwave methods. *Ceramics International* **2013**, *39*, 2283–2292.
 48. Zhang, S.; Long, S.; Li, H.; Xu, Q. A high-capacity organic cathode based on active N atoms for aqueous zinc-ion batteries. *Chemical Engineering Journal* **2020**, *400*, 125898.
 49. Zhang, H.; Xie, S.; Cao, Z.; Xu, D.; Wang, L.; Fang, H.; Shen, J.; Ye, M. Extended π -conjugated system in organic cathode with active C=N bonds for driving aqueous zinc-ion batteries. *ACS Applied Energy Materials* **2021**, *4*, 655–661.
 50. Wu, X.; Hong, J. J.; Shin, W.; Ma, L.; Liu, T.; Bi, X.; Yuan, Y.; Qi, Y.; Surta, T. W.; Huang, W. Diffusion-free Grotthuss topochemistry for high-rate and long-life proton batteries. *Nature Energy* **2019**, *4*, 123–130.

51. Talaie, E.; Bonnick, P.; Sun, X.; Pang, Q.; Liang, X.; Nazar, L. F. Methods and protocols for electrochemical energy storage materials research. *Chemistry of Materials* **2017**, *29*, 90–105.
52. Mizuno, Y.; Okubo, M.; Hosono, E.; Kudo, T.; Zhou, H.; Oh-ishi, K. Suppressed activation energy for interfacial charge transfer of a Prussian blue analog thin film electrode with hydrated ions (Li^+ , Na^+ , and Mg^{2+}). *Journal of Physical Chemistry C* **2013**, *117*, 10877–10882.
53. Kundu, D.; Vajargah, S. H.; Wan, L.; Adams, B.; Prendergast, D.; Nazar, L. F. Aqueous vs. nonaqueous Zn-ion batteries: Consequences of the desolvation penalty at the interface. *Energy & Environmental Science* **2018**, *11*, 881–892.
54. Wang, J.; Polleux, J.; Lim, J.; Dunn, B. Pseudocapacitive contributions to electrochemical energy storage in TiO_2 (anatase) nanoparticles. *Journal of Physical Chemistry C* **2007**, *111*, 14925–14931.
55. Lim, E.; Jo, C.; Kim, H.; Kim, M.-H.; Mun, Y.; Chun, J.; Ye, Y.; Hwang, J.; Ha, K.-S.; Roh, K. C. Facile synthesis of Nb_2O_5 @carbon core-shell nanocrystals with controlled crystalline structure for high-power anodes in hybrid supercapacitors. *ACS Nano* **2015**, *9*, 7497–7505.
56. Wang, W.; Kale, V. S.; Cao, Z.; Kandambeth, S.; Zhang, W.; Ming, J.; Parvatkar, P. T.; Abou-Hamad, E.; Shekhah, O.; Cavallo, L. Phenanthroline covalent organic framework electrodes for high-performance zinc-ion supercapattery. *ACS Energy Letters* **2020**, *5*, 2256–2264.
57. Peng, C.; Ning, G.-H.; Su, J.; Zhong, G.; Tang, W.; Tian, B.; Su, C.; Yu, D.; Zu, L.; Yang, J. Reversible multi-electron redox chemistry of π -conjugated N-containing heteroaromatic molecule-based organic cathodes. *Nature Energy* **2017**, *2*, 17074.
58. Gao, Y.; Li, G.; Wang, F.; Chu, J.; Yu, P.; Wang, B.; Zhan, H.; Song, Z. A high-performance aqueous rechargeable zinc battery based on organic cathode integrating quinone and pyrazine. *Energy Storage Materials* **2021**, *40*, 31–40.
59. Ye, Z.; Xie, S.; Cao, Z.; Wang, L.; Xu, D.; Zhang, H.; Matz, J.; Dong, P.; Fang, H.; Shen, J. High-rate aqueous zinc-organic battery achieved by lowering HOMO/LUMO of organic cathode. *Energy Storage Materials* **2021**, *37*, 378–386.
60. Zhao, Q.; Huang, W. W.; Luo, Z. Q.; Liu, L. J.; Lu, Y.; Li, Y. X.; Li, L.; Hu, J. Y.; Ma, H.; Chen, J. High-capacity aqueous zinc batteries using sustainable quinone electrodes. *Science Advances* **2018**, *4*, eaao1761.
61. Gao, Y.; Li, G.; Wang, F.; Chu, J.; Yu, P.; Wang, B.; Zhan, H.; Song, Z. A high-performance aqueous rechargeable zinc battery based on organic cathode integrating quinone and pyrazine. *Energy Storage Materials* **2021**, *40*, 31–40.
62. Guo, Z.; Ma, Y.; Dong, X.; Huang, J.; Wang, Y.; Xia, Y. An environmentally friendly and flexible aqueous zinc battery using an organic cathode. *Angewandte*

Chemie International Edition **2018**, *57*, 11737–11741.

63. Xu, D.; Cao, Z.; Ye, Z.; Zhang, H.; Wang, L.; John, M.; Dong, P.; Gao, S.; Shen, J.; Ye, M. Electrochemical oxidation of π - π coupling organic cathode for enhanced zinc ion storage. *Chemical Engineering Journal* **2021**, 129245.

64. Liu, N.; Wu, X.; Zhang, Y.; Yin, Y.; Sun, C.; Mao, Y.; Fan, L.; Zhang, N. Building high rate capability and ultrastable dendrite-free organic anode for rechargeable aqueous zinc batteries. *Advanced Science* **2020**, *7*, 2000146.

65. Zhang, H.; Fang, Y.; Yang, F.; Liu, X.; Lu, X. Aromatic organic molecular crystal with enhanced π - π stacking interaction for ultrafast Zn-ion storage. *Energy & Environmental Science* **2020**, *13*, 2515–2523.

66. Zhang, S.; Zhao, W.; Li, H.; Xu, Q. Cross-conjugated polycatechol organic cathode for aqueous zinc-ion storage. *ChemSusChem* **2020**, *13*, 188–195.

67. Wang, Q.; Liu, Y.; Chen, P. Phenazine-based organic cathode for aqueous zinc secondary batteries. *Journal of Power Sources* **2020**, *468*, 228401.

68. Kundu, D.; Oberholzer, P.; Glaros, C.; Bouzid, A.; Tervoort, E.; Pasquarello, A.; Niederberger, M. Organic cathode for aqueous Zn-ion batteries: Taming a unique phase evolution toward stable electrochemical cycling. *Chemistry of Materials* **2018**, *30*, 3874–3881.

69. Kumankuma-Sarpong, J.; Tang, S.; Guo, W.; Fu, Y. Naphthoquinone-based composite cathodes for aqueous rechargeable Zinc-ion batteries. *ACS Applied Materials & Interfaces* **2021**, *13*, 4084–4092.

70. Wang, Q.; Xu, X.; Yang, G.; Liu, Y.; Yao, X. An organic cathode with tailored working potential for aqueous Zn-ion batteries. *Chemical Communications* **2020**, *56*, 11859–11862.

71. Khayum, A.; Ghosh, M.; Vijayakumar, V.; Halder, A.; Nurhuda, M.; Kumar, S.; Addicoat, M.; Kurungot, S.; Banerjee, R. Zinc ion interactions in a two-dimensional covalent organic framework based aqueous zinc ion battery. *Chemical Science* **2019**, *10*, 8889–8894.

72. Wang, W.; Kale, V. S.; Cao, Z.; Lei, Y.; Kandambeth, S.; Zou, G.; Zhu, Y.; Abouhamad, E.; Shekhah, O.; Cavallo, L. Molecular engineering of covalent organic framework cathodes for enhanced zinc-ion batteries. *Advanced Materials* **2021**, 2103617.

73. Dawut, G.; Lu, Y.; Miao, L.; Chen, J. High-performance rechargeable aqueous Zn-ion batteries with a poly (benzoquinonyl sulfide) cathode. *Inorganic Chemistry Frontiers* **2018**, *5*, 1391–1396.

74. Sun, T.; Li, Z. J.; Zhi, Y. F.; Huang, Y. J.; Fan, H. J.; Zhang, Q. Poly (2, 5-dihydroxy-1,4-benzoquinonyl sulfide) as an efficient cathode for high-performance aqueous zinc–organic batteries. *Advanced Functional Materials* **2021**, *31*, 2010049.

75. Zhang, H.; Xu, D.; Wang, L.; Ye, Z.; Chen, B.; Pei, L.; Wang, Z.; Cao, Z.; Shen, J.; Ye, M. A polymer/graphene composite cathode with active carbonyls and secondary amine moieties for high-performance aqueous Zn-organic batteries involving dual-ion mechanism. *Small* **2021**, 2100902.
76. Jiang, B.; Huang, T.; Yang, P.; Xi, X.; Su, Y.; Liu, R.; Wu, D. Solution-processed perylene diimide-ethylene diamine cathodes for aqueous zinc ion batteries. *Journal Colloid and Interface Science* **2021**, 598, 36–44.